Chemical Engineering Journal 527 (2026) 171940

Contents lists available at ScienceDirect

Chemical Engineering Journal

journal homepage: www.elsevier.com/locate/cej

DEM informed surrogate modelling for PBM in fluidized beds

Gero Stoeckl [a,*], Stefan Bellinghausen [b], Stefan Heinrich [a]

[a] Hamburg University of Technology (TUHH), Institute of Solids Process Engineering and Particle Technology, Denickestrasse 15, 21073, Hamburg, Germany
[b] Siemens, Hammersmith Grove 26-28, London, W6 7HA, United Kingdom

1. Introduction

Fluidized bed agglomeration is a widely used particle processing technique. Owing to its versatility and ability to achieve high-throughput production of particles with defined characteristics, fluidized-bed spray-granulation and agglomeration are key unit operations in the food, fine-chemical and pharmaceutical sectors. They facilitate the generation of powders that are devoid of dust and exhibit flowability, which is crucial as these characteristics also affect heat and mass transfer [1–3]. Agglomeration is frequently employed in pharmaceutical manufacturing for several key purposes: (i) improving the flowability, porosity and uniformity of powders; (ii) preventing segregation; (iii) controlling drug release rates and (iv) reducing dust generation [4]. Agglomeration in fluidized beds influences product while simultaneously removing excess moisture from the particles in a single step, thereby increasing their mechanical strength for downstream handling operations such as tableting [5].

The size and structure of the final product can be affected by several parameters that also influence the fluidized bed agglomeration process [6]. Agglomeration denotes the process of uniting primary particles to create larger, porous secondary particles named agglomerates [7]. A fluid bed granulator involves multiple concurrent physical mechanisms, including: (i) the atomization of liquid into fine droplets, (ii) the evaporation of droplets, (iii) the deposition of droplets onto particle surfaces, (iv) the drying of particles and (v) the formation of agglomerates from wet particles [8–11].

The Discrete Element Method (DEM) is an essential tool for analyzing particle flow dynamics and particle-scale characteristics, as it provides a detailed description of inter-particle interactions [5,12–14]. Understanding agglomeration processes requires an understanding of particle movement and collision dynamics. Although DEM accurately captures the behavior of individual particles, its high computational cost precludes simulation of collision frequencies and particle-growth dynamics in large-scale equipment over extended process times [15,16].

The application of CFD-DEM simulations has been essential for understanding particle behavior in fluidized beds [8,17–27]. Nonetheless, these simulations are even more computationally intensive than standalone DEM simulations, especially when addressing large-scale industrial applications.

PBM efficiently predicts macroscopic process behavior. However, it is constrained in its ability to integrate several system factors and relies on the calibration of unknown parameters [28,29]. PBM provides a framework for illustrating the size distribution and the rate of change in particle populations resulting from various processes, including agglomeration. PBM enables tracking of particle size distributions within flow sheet simulations as a tool to simulate multiple interconnected processes due to its low computational demand.

The aforementioned aspects render the integration of DEM and PBM intriguing for the prediction and modelling of diverse particle dynamics. PBM kernels can be developed to predict particle distributions by utilizing accurate data from DEM regarding system insights (particle velocity, collision frequency, etc.). Literature covers studies that integrate DEM and PBM methods. In several investigations, collision data was derived using DEM simulations and a coalescence kernel was established through one-way coupling [30,31]. One-way coupling has proven useful to other processes such as coating or mixing [32–34]. A one-way DEM–ANN–PBM coupling methodology was utilized to investigate the mechanical properties of agglomerates in a uniaxial compression apparatus [35]. A pseudo-coupled DEM–PBM methodology was utilized to simulate breakage mechanisms [36]. Multiple methodologies for bi-directional coupling have been established to simulate diverse particle processes [37–42]. The reoccurring incorporation of PBM within DEM was successfully executed by multiple authors [38–40]. Several researchers [15,38,43] successfully implemented two-way coupling, primarily utilizing PBM and occasionally employing DEM.

The integration of DEM and PBM in a unified framework remains challenging owing to differences in spatial and temporal scales, the complexity of the coupling and the disparity in computational cost. To address these challenges, this study employs CFD-DEM simulations to generate surrogate models that capture fundamental particle-wetting and velocity dynamics, which are key factors governing agglomeration. In the context of this study, the term “surrogate models” refers to classic (CFD-)DEM-derived closure correlations and not machine

* Corresponding author.
E-mail address: gero.stoeckl@tuhh.de (G. Stoeckl).

https://doi.org/10.1016/j.cej.2025.171940
Received 11 October 2025; Received in revised form 3 December 2025; Accepted 14 December 2025
Available online 18 December 2025

Nomenclature

Latin symbols

A	Area
Ar	Archimedes number
b	Fragment size distribution
B	Birth rate
C	Constant
Cp	Specific heat capacity
d	Diameter
D	Death rate / Diffusion coefficient
e	Restitution coefficient
f	Fraction
F	Force
g	Gravitational constant
G	Shear modulus
h	Height
H	Enthalpy
I	Moment of inertia
k	Stiffness
K	Rate constant
m	Mass
M	Torque
MW	Molecular weight
n	Number density distribution
Nu	Nusselt number
p	Pressure
Pr	Prandtl number
q	Power law exponent
r	Radius
R	Rate
Re	Reynolds number
S	Source
Sc	Schmidt number
Sh	Sherwood number
t	Time
T	Temperature
u	Velocity (CFD-DEM) / Particle volume (PBM)
v	(Agglomerate) volume
V	(Control) volume
x	Internal coordinates
X	Mass loading
Y	Young's modulus (DEM) / Volume loading (PBM)

Greek letters

α	Volumetric fraction / Water activity
β	Placeholder (DEM) / Agglomeration rate (PBM)
δ	Overlap
η	Relative moisture content
λ	Thermal conductivity
μ	Friction coefficient (DEM) / Dynamic viscosity (PBM)
ν	Poisson's ratio (DEM) / Kinematic viscosity (PBM) / Single particle drying curve (PBM)
π	Mathematical constant
ρ	Density
τ	Torque (DEM) / Stress tensor (CFD) / Normalized Residence time (PBM)
ψ	Success factor
ω	Angular velocity

Abbreviations

CFD	Computational fluid dynamics
DEM	Discrete element method
PBM	Population balance model
PSD	Particle size distribution

Superscripts

*	Equivalent
d	Damping
geom	Geometric
phys	Physical

Subscripts

0	Initial / Superficial
break	Breakage
c	Contact
cr	Critical
con	Consolidation
coal	Coalescence
cum	Cumulative
d	Droplet
dis	Discrete
E	Environment
eq	Equilibrium
f	Fluid (CFD-DEM) / Frequency (PBM)
i	First (particle)
in	Inlet
j	Second (particle)
kin	Kinetic
g	Gravity (DEM) / Gas (PBM)
gt	Glass transition
L	Liquid
lay	Layering
M	Momentum exchange
mf	Minimum fluidization
Mat	Material
min	Minimum
n	Normal
nc	Non-contact
norm	Normalized
out	Outlet
p	Particle
pen	Penetration
r	Rolling
rel	Relative
res	Residence
s	Sliding
sat	Saturation
S	Solid
sim	Simulation
spray	Spray
t	Tangential
V	Vapour
wet	wetting
W	Wall

learning models.

Additionally, there is a need for more mechanistic agglomeration kernels that can precisely depict the intricate physics of particle agglomeration. More recent kernels tend to rely on mathematical kernels, such as polynomial approximations [44]. This study proposes a novel agglomeration success factor that explicitly incorporates material properties into its formulation. This success factor addresses key limitations of existing models by incorporating material properties (e.g., glass transition temperature) and process dynamics (e.g., spray liquid distribution).

Agglomeration modelling has undergone significant evolution, yet many existing approaches remain constrained by theoretical assumptions, limited validation and narrow applicability. Multi-dimensional PBM and multi-compartment frameworks, which often remain theoretical, are inadequate for practical applications due to high complexity and increased computational demand. While some studies [45] have validated models against individual experiments, they fail to integrate critical phenomena like heat and mass transfer into the agglomeration behavior. Consequently, their range of applicability remains limited. This was extended in a later study to a validation across five experiments [46] and it was demonstrated that the Kapur kernel [47] coefficients could be adjusted universally. However, this study revealed a notable independence of agglomeration behavior on process parameters, while the material system in this study showed a high dependence on process parameters, underscoring the need for models that incorporate these effects comprehensively.

Thermal kernels exist [9,10,48], describing the complexity of binder-based agglomeration appropriately. However, implementation remains challenging due to the highly complex CFD-DEM simulations required, particularly to capture the full physics of the liquid spray. This kernel is primarily applicable to systems governed by liquid bridge formation.

Stokes' mechanistic success criterion connects process parameters such as the spray rate and inlet temperature to binder physics by considering heat and mass transfer via liquid film [49,50]. This is a commonly used criterion to describe the agglomeration probability. However, the Stokes criterion fails to describe agglomeration behavior under extremely high-viscosity conditions ($10^8 - 10^9\ Pa \bullet s$ [51]), as observed in the maltodextrin-water system investigated in this study.

A critical gap in current models lies in their treatment of binder physics and material properties. Many kernels, including [48], focus on binder concentration, effectively excluding water-based systems that are common in the food industry.

One study [50] adequately addresses the rapid penetration of liquid into particles, which alters viscosity dynamics in systems with amorphous materials. Contrary to common assumptions, viscosity initially decreases with liquid addition and subsequently rises during drying, creating a distinct agglomeration mechanism.

Furthermore, the Stokes criterion applies a binary criterion for all particles in a size class. For the material system in this study the authors expect a probability ranging from 0 to 100 % as not all collisions are ideal.

Finally, most models in the literature remain theoretical and are rarely applied to real processes including calibration and validation with experimental data.

This study provides experimental data on maltodextrin agglomeration in a pilot-scale fluidized bed and uses the data to calibrate and validate newly developed models across a wide range of process parameters. The identified gaps in existing approaches are addressed by introducing a novel glass-transition-based success criterion and surrogate models derived from CFD-DEM simulations. These surrogate models supply information that is experimentally inaccessible while keeping computational costs low. The CFD-DEM setup is designed for rapid deployment in industrial applications.

2. Theory

2.1. DEM

Particle motion comprises translational and rotational components, resulting in six degrees of freedom per particle. Particle acceleration is determined using Newton's second law and numerically integrated to obtain velocity and position:

$$m\frac{d\vec{u}}{dt} = \vec{F}_g + \vec{F}_c + \vec{F}_{nc} \tag{1}$$

m represents the mass of the particle, $\vec{u}$ denotes the linear velocity of the particle and $\vec{F}_g$ signifies the gravitational force acting on the particle. $\vec{F}_c$ and $\vec{F}_{nc}$ correspond to the resulting contact and non-contact forces respectively, which occur between particles or between a particle and a wall. t refers to time. Rotational acceleration is obtained as follows:

$$I\frac{d\vec{\omega}}{dt} = \vec{M} \tag{2}$$

I represents the moment of inertia of the particle, ω denotes the angular velocity of the particle and M signifies the resulting contact torque acting on the particle. The normal force $\vec{F}_n$ is expressed as:

$$\vec{F}_n = \frac{4}{3}Y^*\sqrt{r^*}\vec{\delta}_n^{\frac{3}{2}} \tag{3}$$

Y^* and r^* are the equivalent Young's modulus and the equivalent particle radius, respectively. Meanwhile, δ_n represents the normal overlap between the particles. The damping force $\vec{F}_n^d$ in the normal direction is given as:

$$\vec{F}_n^d = -2\sqrt{\frac{5}{6}}\beta\sqrt{k_n m^*}\vec{u}_n^{rel} \tag{4}$$

m^* denotes the equivalent mass of the particles, u_n^{rel} is the normal component of relative velocity and k_n represents the normal stiffness:

$$k_n = 2Y^*\sqrt{r^*\vec{\delta}_n} \tag{5}$$

The equivalent Young's modulus Y^* is defined as:

$$\frac{1}{Y^*} = \frac{1-\nu_i^2}{Y_i} + \frac{1-\nu_j^2}{Y_j} \tag{6}$$

Y_i and Y_j signify the Young's modulus of the two particles and ν is the Poisson's ratio. The equivalent radius r^* is defined as:

$$r^* = \frac{r_i r_j}{r_i + r_j} \tag{7}$$

r_i and r_j denote the radii of two particles in contact. For particle-wall contact, r^* is equal to r_i as r_j approaches infinity. The scaling parameter β is defined as:

$$\beta = -\frac{ln(e)}{\sqrt{\ln^2(e)+\pi^2}} \tag{8}$$

whereby e indicates the coefficient of restitution. The equivalent mass m^* is given as:

$$m^* = \frac{m_i m_j}{m_i + m_j} \tag{9}$$

m_i and m_j denote their respective masses. The tangential force F_t depends on the tangential stiffness k_t and tangential overlap δ_t:

$$\vec{F}_t = -k_t\vec{\delta}_t \tag{10}$$

The tangential damping force $\vec{F}_t^d$ is denoted as:

$$\vec{F}_t^d = -2\sqrt{\frac{5}{6}}\beta\sqrt{k_t m^*}\vec{u}_t^{rel} \tag{11}$$

u_t^{rel} represents the relative tangential velocity. The tangential stiffness k_t is:

$$k_t = 8G^*\sqrt{r^*\vec{\delta}_n} \tag{12}$$

G^* refers to the equivalent shear modulus:

$$\frac{1}{G^*} = \frac{2(2-\nu_i)(1+\nu_i)}{Y_i} + \frac{2(2-\nu_j)(1+\nu_j)}{Y_j} \tag{13}$$

Static and sliding friction $\vec{F}_s$ are defined as:

$$\vec{F}_s = \mu_s \vec{F}_n \tag{14}$$

μ_s represents the coefficient of static or sliding friction. Rolling friction $\vec{\tau}_r$ is defined as:

$$\vec{\tau}_r = -\mu_r \vec{F}_n r_i \omega_i \tag{15}$$

μ_r refers to the rolling friction coefficient. In addition to normal contributions, sliding and rolling resistances are also considered. Sliding resistance acts in the tangential direction, with the tangential force being limited by the Coulomb criterion.

2.2. CFD-DEM

CFD-DEM simulations typically apply the finite volume method to solve the Navier-Stokes equations, providing a velocity field $\vec{u}$ and a pressure field p that are discretized over a grid of control volumes:

$$\frac{\partial\left(\alpha_f \rho_f \vec{u}_f\right)}{\partial t} + \nabla\cdot\alpha_f \rho_f \vec{u}_f \vec{u}_f = -\alpha_f\nabla p + \alpha_f\nabla\cdot\vec{\tau} + \alpha_f \rho_f \vec{g} + \dot{S}_M \tag{16}$$

α signifies the volumetric phase fraction of the fluid phase, $\vec{\tau}$ the stress tensor, ρ the fluid density, g the gravitational acceleration and S_M refers to the momentum exchange term. The continuity equation is defined as:

$$\frac{\partial(\alpha_f\rho_f)}{\partial t} + \nabla\cdot\alpha_f \rho_f \vec{u}_f = 0 \tag{17}$$

2.3. PBM

The population balance equation can be expressed in either 1-D or multi-D form, where the dimensionality is determined by the number of properties of interest, represented by the vector $\vec{x}$. The control volume, denoted as V, represents the region where the population balance analysis is conducted. The variable n refers to the volume-specific number density of particles, while $\vec{x}$ is the set of granule properties of interest and t represents time. The volumetric flow rates entering and leaving the control volume are represented by $\dot{V}_{in}$ and $\dot{V}_{out}$, respectively. Additionally, the terms $\dot{B}$ and $\dot{D}$ represent the volume-specific birth and death rates due to processes such as nucleation, coalescence and breakage, which cause discrete changes in the properties of particles. The term $\frac{\partial}{\partial\vec{x}}\left(Vn(\vec{x},t)\frac{d\vec{x}}{dt}\right)$ accounts for continuous changes in particle properties that arise from rate processes such as consolidation and layering.

An inherent assumption in PBM is that the equipment operates under ideal mixing and that the process conditions remain homogeneous. The PSD is tracked through the number density n in every size class over time t [52]:

$$\frac{\partial Vn(\vec{x},t)}{\partial t} + \frac{\partial}{\partial\vec{x}}\left(Vn(\vec{x},t)\frac{d\vec{x}}{dt}\right) = \dot{V}_{in}n_{in}(\vec{x},t) - \dot{V}_{out}n_{out}(\vec{x},t) + V\left(\dot{B}(\vec{x},t) - \dot{D}(\vec{x},t)\right) \tag{18}$$

A one-dimensional (1-D) PBM approach is employed to monitor product properties. The primary focus is the granule diameter, which is discretized into size classes for detailed analysis, while all other properties are averaged. Using the lumped parameter approach [53], properties such as liquid volume and void volume are specifically tracked and averaged within a single size bin to account for size dependency. Other properties are derived from those that are tracked:

$$\frac{\partial Vn(v,t)}{\partial t} + \frac{\partial}{\partial v}\left(Vn(v,t)\left(\dot{G}_{lay} + \dot{G}_{con}\right)\right) = \dot{V}_{in}n_{in}(v) - \dot{V}_{out}n_{out}(v) + V\left(\dot{B}_{nuc}(v) + \dot{B}_{coal}(v) + \dot{B}_{break}(v) - \dot{D}_{coal}(v) - \dot{D}_{break}(v)\right) \tag{19}$$

The terms $\dot{G}_{lay}$ and $\dot{G}_{con}$ represent the rate of change due to layering and consolidation. The terms $\dot{B}_{nuc}$, $\dot{B}_{coal}$ and $\dot{B}_{break}$ are the birth rates for nucleation, coalescence and breakage, while $\dot{D}_{coal}$ and $\dot{D}_{break}$ represent the death rates due to coalescence and breakage [54].

However, in the context of fluidized bed agglomeration of maltodextrin, the effects of nucleation, layering and consolidation are negligible and can therefore be excluded from the equation. Secondary nucleation can be neglected because fines are removed from the system prior to the experiments. Layering is negligible because water evaporates without leaving a residue on the particles. Consolidation can be excluded due to the low stresses in a fluidized bed and the increase in bulk density during agglomeration. The terms for the flow rates in and out of the process volume are removed as the system is a batch process:

$$\frac{\partial Vn(v,t)}{\partial t} = V\left(\dot{B}_{coal}(v) + \dot{B}_{break}(v) - \dot{D}_{coal}(v) - \dot{D}_{break}(v)\right) \tag{20}$$

The coalescence birth rate is a function of the agglomeration rate β:

$$\dot{B}_{\text{coal}}(v) = \frac{1}{2}\int_0^v \beta(v-u,u)n(v-u)n(u)du \tag{21}$$

The pre-factor $\frac{1}{2}$ avoids accounting twice for the same particle. The integral starts from the smallest possible particle volume 0 to the agglomerate volume v, since either partner can not be larger than the resulting agglomerate. The agglomerate volume ν is equal to the two colliding particles $(\nu - u)$ and u:

$$\nu = (\nu - \mathrm{u}) + \mathrm{u} \tag{22}$$

The breakage birth rate $\dot{B}_{break}$ depends on the discretized fragment size distribution b and the breakage rate K_{break}:

$$\dot{B}_{break}(\nu) = \int_\nu^\infty b(\nu,u)K_{break}(u)n(u)du \tag{23}$$

A fragment volume cannot be larger than a parent particle whose volume is ν. In theory, the upper limit ∞ refers to the largest particles

but in practice it is limited to the maximum expected agglomerate volume. The coalescence death rate $\dot{D}_{coal}$ also depends on the agglomeration rate β:

$$\dot{D}_{coal}(\nu) = \int_0^{\infty} \beta(\nu,u)n(\nu)n(u)du \tag{24}$$

The breakage death rate $\dot{D}_{break}$ only depends on the breakage rate K_{break}:

$$\dot{D}_{break}(\nu) = K_{break}(\nu)n(\nu) \tag{25}$$

The discretized fragment size distribution b_{dis} is determined from the cumulative fragment size distribution b_{cum}:

$$b_{dis}(\nu,u) = \frac{db_{cum}(\nu,u)}{du} \tag{26}$$

3. Methodology

3.1. Experimental

3.1.1. Material

In this study, food-grade maltodextrin (Avebe MD20P) with a dextrose content of approximately 19 wt% was used. Derived from the enzymatic breakdown of potato starch, this polysaccharide was chosen for its excellent solubility and functional properties, making it a common model material in the food industry. To ensure consistency and preserve its integrity, the maltodextrin was sourced from a single batch and stored under controlled temperature and humidity conditions. The material properties are described in detail in [55].

3.1.2. Lab scale fluidized bed

The study employs a GF3 lab scale fluidized bed (Glatt GmbH, Germany) in a top-spray configuration. The setup features an 18 cm diameter air distributor plate with a 105 µm mesh size. A Series 970-S4 spray nozzle (Düsen-Schlick GmbH) with a 1.2 mm orifice and level 3 air cap produces droplets with a median diameter ($d_{50,3}$) of 33 µm and a spray angle of approximately 50°. The nozzle is positioned 25 cm above the distributor plate, operating at 2 bar air pressure. Water is supplied via a peristaltic pump and experiments are conducted in batch mode using 0.5 kg bed mass. The lab scale fluidized bed setup is extensively explained in [55].

3.1.3. Pilot scale fluidized bed

The fluidized bed utilized in this study is the GF25 pilot scale fluidized bed with internal filters manufactured by Glatt GmbH, Germany. A schematic representation of the device is depicted in Fig. 1. The fluidized bed inlet shape is rectangular with a width and depth of 1 m and 0.25 m respectively. The fluidized bed consists of four chambers that can be separated with weirs and operates in a top-spray configuration with two sprays. The nozzle air is supplied at a pressure of 2 bar (absolute). The nozzle configuration comprises a GKWZ 2.10 (Duesen-Schlick GmbH, Germany) equipped with a liquid nozzle diameter of 3 mm, along with its accompanying air cap. The spray setting yields droplets of size 30 μm and a spray angle of approximately 50°. Experiments are

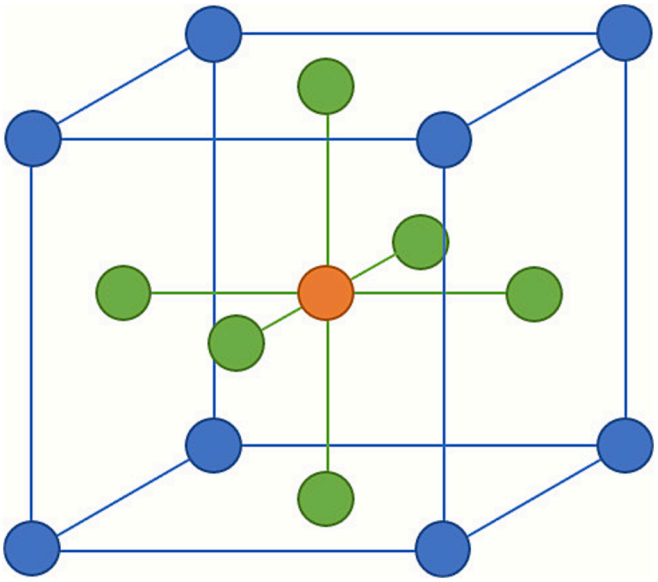

Fig. 2. Experimental design: (i) corner points in blue, (ii) face center points in green and (iii) volume center point in orange.

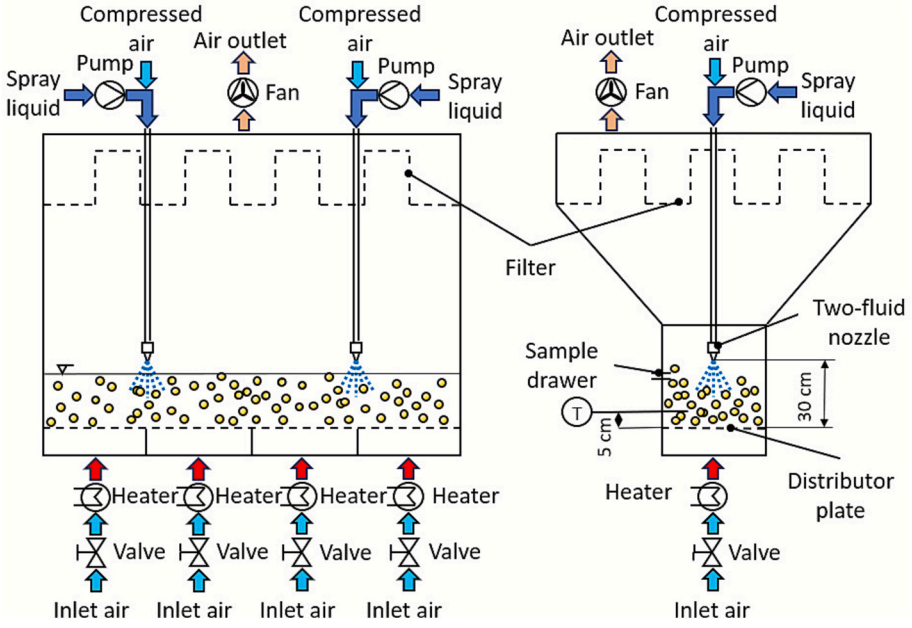

Fig. 1. Schematic representation of the pilot scale fluidized bed set-up showing: front view (left) and side view (right).

Table 1
Process parameters for pilot scale batch agglomeration experiments.

Inlet air flow rate [$m^3\ h^{-1}$]	Inlet air temperature [°C]	Spray rate [$g\ min^{-1}$]
600	40	60
700	60	90
800	100	120

performed in batch mode with a bed mass of 15 kg.

The filters are cleaned by reversing the flow direction through each individual filter for a duration of 6 s at a pressure of 4 bar. The filter cleaning operation is conducted every 1.5 min. Samples are drawn after cleaning the filters. The sample drawer is positioned 30 cm above the distributor plate.

3.1.4. Design of experiment

The design of experiments from the lab scale fluidized bed from [55] is adjusted to gain similar conditions in the process chamber (Fig. 2). The two-phase approach for the design of experiments is maintained, resulting in process parameters shown in Table 1.

The inlet velocity of lab and pilot scale device are the same to ensure similar fluidization regime and characteristics. The inlet air temperature is also kept at the same values. The spray liquid flow rate is scaled based on a simple heat balance to maintain the same enthalpy ratio of spray liquid to inlet air. The combination of high inlet air temperature and high spray rate is included to probe the upper part of the operating window where overwetting and bed collapse risks are highest, while remaining within a stable fluidization regime as confirmed in preliminary trials. The nozzle geometry is chosen to match a similar droplet size. This results in a three-level parameter set as shown in Table 1.

This design yields a cumulative of 15 individual experiments. The model is calibrated with 8 corner points and validated with the 6 points in the cube faces, 2 randomly chosen corner points and the center point. 252 sample points were utilized to calibrate and validate the model.

3.2. Numerical

Surrogate models are essential tools in computational modelling to approximate complex systems with simplified representations. In this chapter, the term “surrogate models” specifically denotes DEM-informed closure correlations for spray-zone residence time, particle velocity and solid holdup, which are derived from CFD–DEM simulations and then used inside the PBM. This chapter outlines workflow surrogate model development, involving key stages such as calibration of CFD-DEM with element tests, deriving surrogate models from CFD-DEM simulations and integrating them in PBM (Fig. 3). Additionally, fluidized bed experiments are used to calibrate and validate the improved PBM framework. The CFD-DEM simulation setup is explained in more detail in chapter 3.2.1.2. The PBM setup and the calibration of the PBM model parameters are explained in chapter 3.2.2.2. The surrogate model development is explained for the wetting behavior in the following paragraphs.

3.2.1. CFD-DEM

3.2.1.1. Wetting model. Due to the introduction of the glass transition, which is heavily dependent on the particle moisture content, it is necessary to get a more accurate model for the liquid distribution of the spray. The basis of this model is the thorough study conducted by CFD-DEM simulations, specifically designed to investigate the dynamics within a predetermined cylindrical spray zone. These simulations are an essential tool for comprehending the complex relationship between fluid dynamics and particle interactions that are fundamental to the wetting process. The liquid distribution cannot be measured using experiments. By using CFD-DEM simulations it is possible to represent the correct trend of the liquid distribution with respect to particle size under consideration of different inlet velocities. Residence time reflects the time spent by a particle in the spray zone therefore being exposed to the liquid. In the CFD–DEM simulations only the gas–solid flow is resolved, droplets are not explicitly injected. Instead, liquid physics such as spray deposition, evaporation and subsequent drying are represented at the PBM level through wetting and drying closures, which use the DEM-derived residence times, velocities and solid holdup as inputs.

The simulations are pre-run to establish a steady state of the fluidization behavior. The residence time is then tracked over multiple seconds and the arithmetic mean average over all particles of the same size is determined:

$$t_{res,i} = \frac{\sum_N t_{N,i}}{n_{p,i}} \tag{27}$$

The mean residence time is then normalized with the simulation time to gain the dimensionless residence time τ:

$$\tau_i = \frac{t_{res,i}}{t_{sim}} \tag{28}$$

A linear model for the dimensionless residence time as a function of Reynolds number *Re* is derived:

$$\tau_i = C_1 Re_i + C_2 \tag{29}$$

The dimensionless Reynolds number *Re* is a function of the gas inlet velocity $u_{g,inlet}$, particle minimum fluidization velocity u_{mf}, particle size d and gas viscosity ν_g:

$$Re_i = \frac{\left(u_{g,inlet} - u_{mf}\right)^* d_i}{\nu_g} \tag{30}$$

The minimum fluidization velocity is determined from the Reynolds number at minimum fluidization velocity Re_{mf}:

$$u_{mf,i} = Re_{i,mf}{}^* \frac{\nu_g}{d_i} \tag{31}$$

The Reynolds number at minimum fluidization velocity is determined with the correlation of [56]:

$$Re_{i,mf} = \frac{-1650 + \sqrt{1650^2 + 4^*24.5^*Ar_i}}{2^*24.5} \tag{32}$$

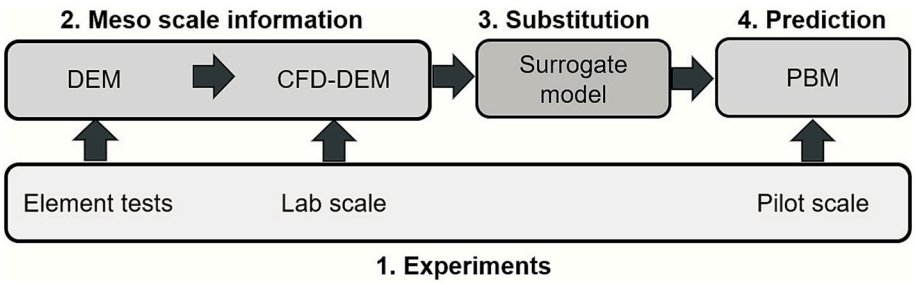

Fig. 3. Workflow for surrogate-model development.

The dimensionless Archimedes number Ar is a function of the particle density ρ_p, particle size d, difference between the particle and gas density $(\rho_p - \rho_g)$, gravity constant g and gas viscosity μ:

$$Ar_i = \frac{\rho_g d_i^3 (\rho_p - \rho_g) g}{\mu^2} \tag{33}$$

The predicted dimensionless residence time is normalized overall size classes:

$$\tau_{norm,i} = \frac{\tau_i}{\sum_i \tau_i} \tag{34}$$

The liquid injection flow rate $\dot{m}_{deposition}$ together with the surface area based liquid distribution gives the wetting rate of each size class i:

$$\dot{m}_{deposition,i} = \frac{\tau_i d_i^2}{\sum_i \tau_i d_i^2} \dot{m}_{deposition} \tag{35}$$

The spray zone volume, position and shape are approximated by visual observation of the spray cone during the experiments (Fig. 4):

3.2.1.2. Setup. CFD-DEM simulations were performed using the software CFDEMcoupling [57] which couples LIGGGHTS [58] with OpenFOAM [59].

The meshing was conducted using snappyHexMesh, a hexahedral cut-cell mesher, within OpenFOAM. The lengths of the sides of the cells are provided in Table 2 and the final mesh is displayed in Fig. 5.

The time step for DEM is selected as 15 % of the Rayleigh and Hertzian time. The CFD time step adheres to the Courant-Friedrich-Lewy criterion. The time step is adjusted to keep the Courant number below 1. The particle and wall material and contact properties together with the numerical specifications are given in Table 2. The DEM material parameters are calibrated with standardized experiments for bulk density, angle of repose and dynamic angle of repose. The CFD-DEM drag is calibrated to match the pressure drop at minimum fluidization velocity.

The Young's modulus of particles was reduced to allow for larger time steps and a reduction in computation time. The density was set to approximate the envelope density of the material. Contact forces are calculated according to the Hertz-Mindlin-Tsuji law [60]. The rolling

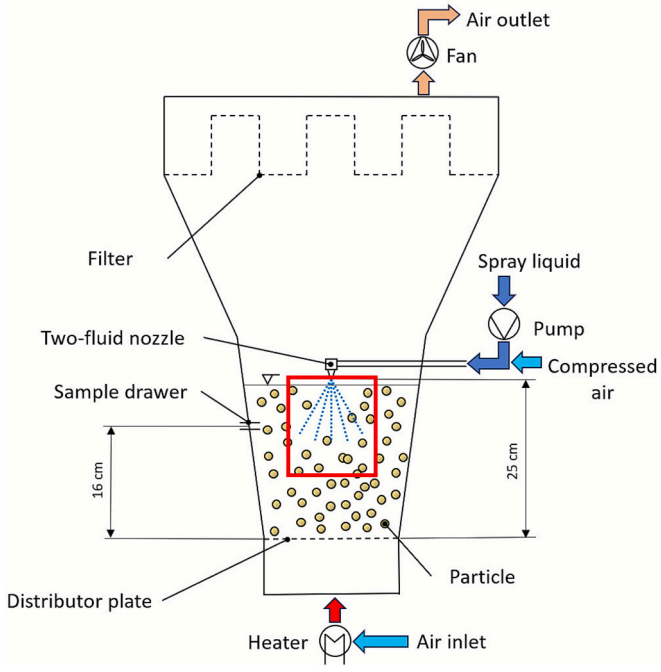

Fig. 4. Schematic representation of the cylindrical spray zone (red) in the lab scale fluidized bed.

Table 2
Numerical settings and particle and wall properties of CFD-DEM setup.

Parameter	Units	Value
Numerics		
Time step CFD	s	5E-04
Time step DEM	s	1E-05
Coupling interval	–	50
Particle scaling factor	–	8
Particle & wall		
Diameter	µm	PSD 1–6
Density	kg m^{-3}	900
Young's modulus p	Pa	1E+06
Young's modulus w	Pa	5E+08
Poisson ratio	–	0.25
Restitution coefficient p-p	–	0.7
Restitution coefficient p-w	–	0.7
Friction coefficient p-p	–	0.3
Friction coefficient p-w	–	0.3
Rolling friction coefficient p-p	–	0.05
Rolling friction coefficient p-w	–	0.05
Mesh		
Cell size	m	0.01

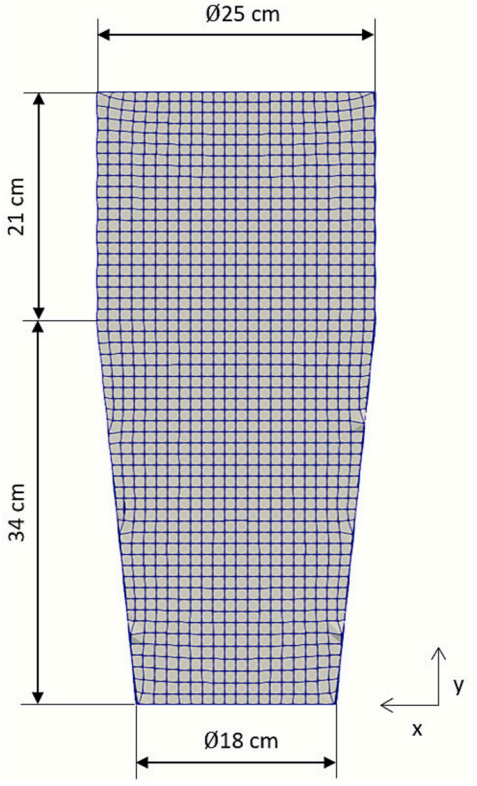

Fig. 5. Mesh of conical process chamber of lab scale fluidized bed GF3. The mesh cell size equals 2.5d_p.

Table 3
Particle size distributions for CFD-DEM.

Diameter [µm]	PSD 1	PSD 2	PSD 3	PSD 4	PSD 5	PSD 6
d_1	97	119	140	162	184	205
d_2	137	171	204	237	271	304
d_3	173	217	261	306	350	395
d_4	220	279	337	395	453	511
d_5	326	412	499	585	671	757

friction is described with the elastic plastic spring dashpot torque model (epsd2) [61]. The drag forces are calculated using the model of Beetstra [62]. The number of particles with the PSD displayed in Table 3 yields too many particles to simulate. Therefore, a particle scaling factor of 8 is applied. The 5 size classes in each PSD are weighted equally with 20 wt %. The interaction parameters for particle-particle and particle-wall interactions are assumed to be the same as the walls are quickly covered in a thin powder layer.

DEM material parameters impact particle dynamics and with that agglomeration probability. The restitution coefficient influences normal energy dissipation during collision, while friction and rolling-resistance coefficients contribute to tangential and rotational momentum exchange and energy dissipation. Together, these parameters influence collision frequency, collision velocity and contact time of colliding particles.

18 simulations are executed as listed in Table 4. The simulations vary the PSD from Table 3 and the inlet velocity matching the experiments upper and lower limits and a center point.

3.2.2. PBM

The following chapters introduce a success factor based on the most relevant material properties to the agglomeration mechanism and the PBM setup it is embedded in. Unlike the commonly used Stokes criterion, this success factor is not based on mechanical energy dissipation, but rather on the influence of process conditions on the material properties.

3.2.2.1. Glass transition success factor. The agglomeration rate β consists of the collision frequency in the spray zone $C_{f,spray}$ and the success factor $\psi_{i,j}$. The success factor defines the probability of a collision to be successful:

$$\beta(v,u) = C_{f,spray} {}^{*}\psi_{i,j} \tag{36}$$

The collision frequency $C_{f,spray}$ depends on the rate constant β_0, the EKE kernel (M. [63]) which depends on the particle sizes d_i and d_j and the fraction of particles residing in the spray zone τ_{Spray}. τ_{Spray} equals the dimensionless residence time determined through DEM simulations:

$$C_{f,spray} = \beta_0 \left(d_i + d_j\right)^2 \sqrt{\frac{1}{d_i^3} + \frac{1}{d_j^3}}\, \tau_{spray} \tag{37}$$

The success factor $\psi_{i,j}$ consists of the geometric success factor $\psi_{i,j}^{geom}$ and the physical success factor $\psi_{i,j}^{phys}$. The geometric success factor determines the probability that two colliding particles get in contact on a wetted spot. The physical success factor determines the probability that two colliding particles are in the appropriate physical state to agglomerate:

$$\psi_{i,j} = \psi_{i,j}^{geom} \psi_{i,j}^{phys} \tag{38}$$

When inserting Eqs. (37) and (38) into (36) it results in the overall equation for the agglomeration kernel shown in Eq. (39):

$$\beta_{i,j} = \beta_0 \left(d_i + d_j\right)^2 \sqrt{\frac{1}{d_i^3} + \frac{1}{d_j^3}}\, \tau_{Spray} \psi_{i,j}^{geom} \psi_{i,j}^{phys} \tag{39}$$

The geometric success factor is based on the liquid coverage of the colliding particles $f_{wet,i}$ and $f_{wet,j}$. Considering the three cases: (i) wet-wet, (ii) wet-dry and (iii) dry-wet collisions:

$$\psi_{i,j}^{geom} = 1 - \left(1 - f_{wet,i}\right)\left(1 - f_{wet,j}\right) \tag{40}$$

The liquid surface coverage of a wetted particle $f_{wet,i}$ is determined by using the model of [64]. The liquid coverage depends on the dimensionless coating number ϕ_i:

$$f_{wet,i} = 1 - exp(-\phi_i) \tag{41}$$

The dimensionless coating number is derived from single particle coating experiments and compares the volume of liquid associated with a particle to a characteristic droplet volume projected onto the particle surface. Small values correspond to isolated wet spots and low surface coverage, whereas larger values indicate that multiple droplets overlap and most of the surface is covered. The model does not consider droplets spreading and merging or the effect of the contact angle [64]. The coating number ϕ_i depends on the particle moisture loading X_{LS}, particle diameter d_p, particle envelope density ρ_{env}, the contact area between droplet and particle $A_{contact}$, droplet diameter d_d, droplet liquid density ρ_d and particle surface area $A_{P,i}$:

$$\phi_i = \frac{X_{LS,i} d_i^3 \rho_{env} A_{contact}}{d_d^3 \rho_d A_{P,i}} \tag{42}$$

The particle moisture loading X_{LS} depends on the liquid mass flow rate $\dot{m}_{deposition,i}$ that is deposited on the particles mass flow rate $\dot{m}_{s,sprayzone,i}$ that is passing through the estimated spray zone:

$$X_{LS,i} = \frac{\dot{m}_{deposition,i}}{\dot{m}_{s,sprayzone,i}} \tag{43}$$

The liquid distribution to each size class is derived from the mean residence time in the spray zone, extracted from DEM simulations. The liquid distribution per size class $\dot{m}_{deposition,i}$ is explained in more detail in chapter 3.2.1.1. The liquid spray flow rate assigned to each size class resembles the liquid distribution model applied to the liquid spray rate after evaporation $\left(\dot{m}_{L,in} - \dot{m}_{evap}\right)$:

$$\dot{m}_{deposition,i} = \frac{\tau_i d_i^2}{\sum_i \tau_i d_i^2} \left(\dot{m}_{L,in} - \dot{m}_{evap}\right) \tag{44}$$

The mass flow rate of particles through the spray zone $m_{s,sprayzone}$ is estimated with the average particle mass in the spray zone $m_{s,sprayzone}$ determined in DEM simulations and the estimated time for particles to cross the spray zone once t_{spray}:

$$\dot{m}_{s,sprayzone,i} = \frac{m_{s,sprayzone,i}}{t_{spray,i}} \tag{45}$$

The solid mass of each size class in the spray zone is described as the fraction of the particle bed per size class as follows:

$$m_{s,sprayzone,i} = w_{s,sprayzone,i} {}^{*} m_{s,bed,i} \tag{46}$$

The solid mass fraction of the total mass for each size class in the spray zone $w_{s,sprayzone,i}$ is derived from DEM simulations by averaging over multiple seconds:

Table 4
CFD-DEM simulations with respective parameters.

Case	PSD	Inlet velocity [m s^{-1}]
1	1	0.65
2	2	0.65
3	3	0.65
4	4	0.65
5	5	0.65
6	6	0.65
7	1	0.87
8	2	0.87
9	3	0.87
10	4	0.87
11	5	0.87
12	6	0.87
13	1	1.09
14	2	1.09
15	3	1.09
16	4	1.09
17	5	1.09
18	6	1.09

$$w_{s,sprayzone,i} = C_1{*}Re_i^2 + C_2{*}Re_i + C_3 \quad (47)$$

The model is explained in more detail in the appendix. The residence time of particles to pass through the spray zone once is estimated with the diameter of the spray zone $d_{sprayzone}$ and the average particle velocity in the spray zone $v_{sprayzone}$ determined in DEM simulations:

$$t_{spray,i} = \frac{d_{sprayzone}}{v_{sprayzone,i}} \quad (48)$$

Particle velocity in the spray zone $v_{sprayzone,i}$ is determined as a function of the Reynolds number:

$$v_{sprayzone,i} = C_1{*}Re_i + C_2 \quad (49)$$

The model is explained in more detail in the appendix. The contact area between droplet and particle is assumed to be equal to the cross-sectional area of the droplet. The droplets are assumed to be ideal spheres. The contact area of droplet and particle $A_{contact}$ is determined as follows:

$$A_{contact} = d_d^2{*}\frac{\pi}{4} \quad (50)$$

Particles are assumed to be ideal spheres, therefore the particle surface area A_i is:

$$A_i = d_i^2{*}\pi \quad (51)$$

The physical success factor is based on the stickiness of the particle surface which is a function of the glass transition temperature. When two particles collide on a wet spot there are three cases that need to be considered: (i) sticky-sticky, (ii) sticky-not sticky and (iii) not sticky-sticky:

$$\psi_{i,j}^{phys} = 1 - \left(1 - p_{sticky,i}\right)\left(1 - p_{sticky,j}\right) \quad (52)$$

The probability of a particle to be sticky due to glass transition is defined as a region between the glass transition temperature $T_{gt,i}$ and an artificially set temperature offset above the glass transition temperature (Fig. 6). The region is defined as a linear function with the following properties: the probability for a particle to be sticky $p_{sticky,i}$ at (i) the glass transition temperature is 1 %, (ii) at the so-called sticky region [65], which is about 20 K above the glass transition temperature, 50 % and (iii) at the point of bed collapse [65], which is almost constant at 40 K above the glass transition temperature, 99 %. The equation defining the probability in this region is shown in Eq. (53).

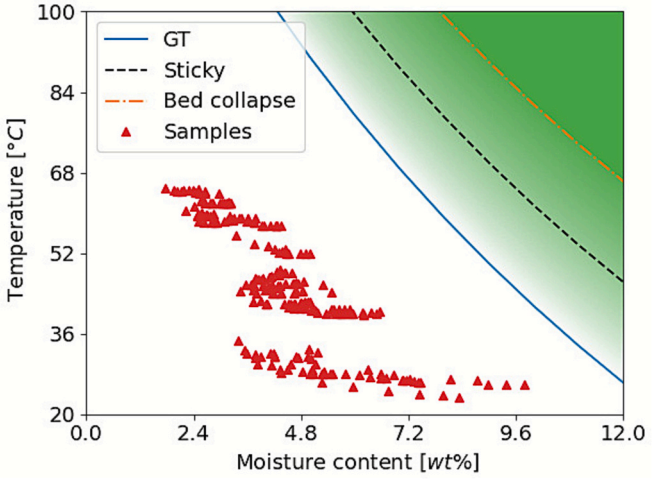

Fig. 6. Agglomeration probability as a function of particle temperature and moisture content. Below the glass transition temperature (GT) the probability for a successful collision is 1 %, increasing to 50 % at the sticky point and to 99 % near bed collapse. The white to green gradient indicates the transition region.

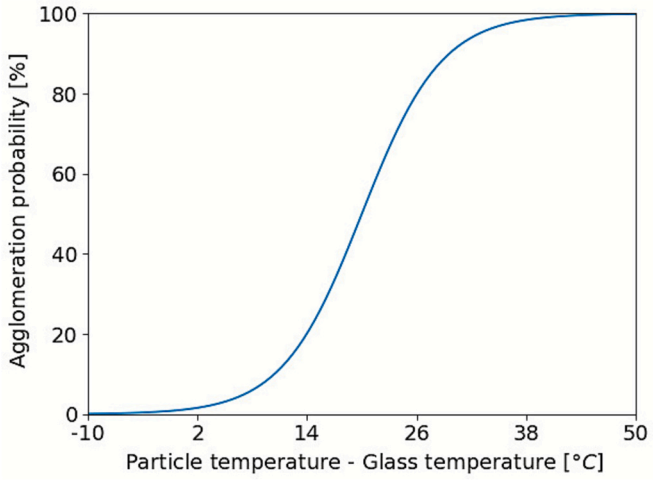

Fig. 7. Agglomeration probability due to stickiness.

This probability is assumed to be a linear function with constants $C_1 = 8.733$ and C_2=20 (sticky temperature offset). The *tanh* is applied for numerical reasons. The particle temperature is denoted as T_i. The probability could be derived from simple single particle collision experiments as outlined in [66]:

$$p_{sticky,i} = 0.5\left(tanh\left(\frac{T_i - \left(C_{2+}T_{gt,i}\right)}{C_1}\right) + 1\right) \quad (53)$$

The probability of a particle to be sticky as a function of the glass transition temperature is displayed in Fig. 7.

The equation describes the glass transition temperature as a function of the glass transition temperature of the pure components $T_{gt,l}$ and $T_{gt,s}$, the mass fractions of liquid x_l and solid x_s and a fitting constant k:

$$T_{gt,i} = \frac{kx_{l,i}T_{gt,l} + \left(1 - x_{l,i}\right)T_{gt,s}}{kx_{l,i} + \left(1 - x_{l,i}\right)} \quad (54)$$

The mass fractions of solid and liquid in particles in the spray zone are determined by considering the added liquid spray flow rate $\dot{m}_{spray,i}$ to the particles passing through the pre-defined spray zone $\dot{m}_{s,exposed,i}$ and the particle bed liquid loading $X_{0,i}$. The assumed spray zone geometry and dimensions are based on visual observation:

$$X_{wetspot,i} = \frac{\dot{m}_{deposition,i}}{\dot{m}_{s,exposed,i}} + X_{0,i} \quad (55)$$

The exposed mass of the total particle mass flowing through the spray zone is defined as the fraction of wetted volume to total volume of a single particle:

$$\dot{m}_{s,exposed,i} = \dot{m}_{s,sprayzone,i}{*}\frac{V_{wet,i}}{V_{particle,i}} \quad (56)$$

The wetted volume of a particle upon droplet deposition is assumed to be a cylinder with the cross-sectional area equal to the wetted surface area expressed by the liquid surface area coverage $f_{wet,i}$ and the particle surface area A_i and a constant liquid penetration depth h_{pen}:

$$V_{wet,i} = h_{pen}{*}A_i{*}f_{wet,i} \quad (57)$$

The liquid penetration depth is calibrated in this study but could be measured in general by balancing diffusion and drying of the wetted particles. In this study instant penetration of liquid before the collision and instant drying down to the level of the average particle bed moisture content per size class after the collision is assumed (Fig. 8).

3.2.2.2. Setup. PBM simulations are executed using the fluid bed granulator model from gProms Formulated Products (Siemens AG,

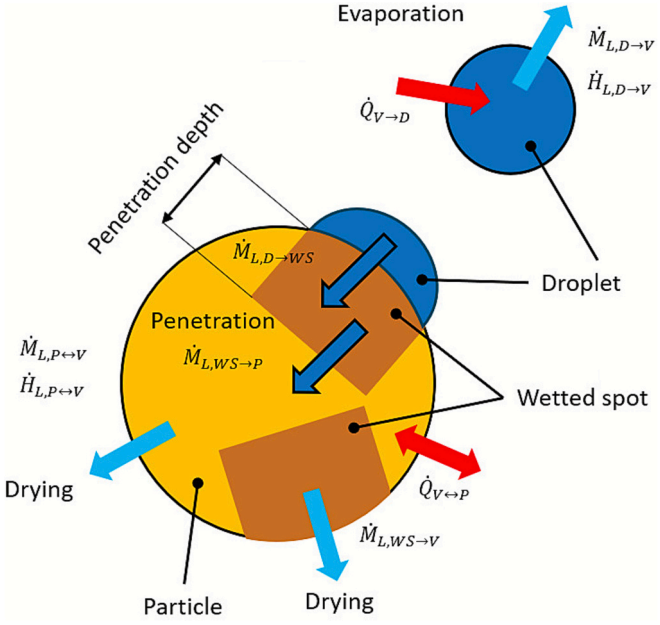

Fig. 8. Heat and mass transfer balances on a single particle.

Table 5
Numerical settings and parameters for the loss function during calibration and validation.

Parameter	Unit	Value
Numerics		
Minimum particle size	µm	50
Maximum particle size	µm	1000
Number of size classes	–	10
Standard deviation		
Solid moisture content	wt%	1
Outlet gas temperature	°C	2
$d_{5,3}$, $d_{10,3}$, $d_{16,3}$, $d_{25,3}$, $d_{50,3}$	%	7
$d_{75,3}$	%	8
$d_{84,3}$	%	9
$d_{90,3}$	%	10
$d_{95,3}$	%	11

Table 6
Reactor dimensions and material specifications for solid, liquid and vapour.

Parameter	Unit	Value
Reactor		
Bed cross sectional area	m^2	0.25
Wall surface area	m^2	7.3
Equipment volume	m^3	1.2
Solid		
Skeletal density	kg m^{-3}	1545
Specific heat capacity	J kg^{-1} K^{-1}	1220
Liquid		
Density	kg m^{-3}	1000
Specific heat capacity	J kg^{-1} K^{-1}	4180
Dynamic viscosity	Pa s	1e-3
Vapour		
Diffusivity	m^2 s^{-1}	2.0e-5
Thermal conductivity	W m^{-1} K^{-1}	2.4e-2

Germany). The wetting model and agglomeration kernel were added as custom submodels. The internal gProms DAEBDF solver [67–69] was utilized with the default settings. Discretization and settings for the loss function can be found in Table 5:

The dimensions of the granulator and the material specifications for solid, liquid and vapour phase are shown in Table 6.

Table 7
Numerical settings, initial conditions and process parameters. "Ind" refers to the individual settings of each experiment.

Parameter	Control type	Unit	Value
Initial conditions: Reactor			
Mass wet air	Time-invariant	kg	1.53
Mass solids	Time-invariant	kg	Ind
Temperature	Initial	°C	Ind
Initial conditions: Environment			
Temperature	Time-invariant	°C	Ind
Initial conditions: Granules			
Bulk density	Time-invariant	kg m^{-3}	560
Intra particle void fraction	Time-invariant	m^3 m^{-3}	0.3
Mass fraction liquid	Initial	w%	Ind
Mass fraction solid	Initial	w%	Ind
Median size	Initial	µm	Ind
Standard deviation	Initial	µm	Ind
Process parameters			
Vapour flow rate	Time-invariant	m^3 h^{-1}	Ind
Vapour temperature	Piecewise-linear	°C	Ind
Vapour absolute humidity	Piecewise-linear	g kg^{-1}	Ind
Spray liquid flow rate	Time-invariant	g min^{-1}	Ind
Spray liquid temperature	Time-invariant	°C	10

The initial conditions and process parameters can be found in Table 7. The simulation is initialized with material properties and process conditions from the time the first sample is drawn, which is also the start of the liquid spray. The initial particle size distribution is a log-normal distribution with parameters fitted using the Excel "Simplex LP" solver. The particle size distribution is then further tracked on a logarithmic grid with 10 size classes.

Non-uniform hydrodynamics of the fluidized bed process are represented implicitly via size- and operating-dependent closure relations (e.g. residence time and holdup in the spray zone) obtained from CFD-DEM simulations. These quantities enter the heat- and mass balance as well as the glass transition success factor and thereby convey the influence of particle dynamics and flow patterns into the 1-D PBM.

The heat- and mass balances between phases and reactor components are shown in Fig. 9. Evaporation refers to droplet evaporation and drying refers to evaporation of liquid on the particles. Vapour is a mixture of inert gas and evaporated components.

Energy and mass balances per size class are described in the following paragraphs. The accumulation of liquid on solids over time depends on the liquid deposition rate $\dot{m}_{deposition,i}$ and the drying rate $\dot{m}_{drying,i}$ of each liquid component i:

$$m_S \frac{dX_i}{dt} = \dot{m}_{deposition,i} - \dot{m}_{drying,i} \tag{58}$$

The energy balance for the solids depends on the deposition and drying of liquid as well as the heat transfer from vapour to solids:

$$\frac{dH_s}{dt} = \sum_{i}^{components} \dot{H}_{deposition,i} - \dot{H}_{drying,i} + \dot{Q}_{V\leftrightarrow S} \tag{59}$$

H_s refers to the accumulated enthalpy in the solid phase:

$$H_s = \rho_p T_S \int_0^{\infty} n(v,t) \left(\sum_{i}^{components} x_i cp_i \right) dv \tag{60}$$

The mass balance for the gas and liquid in the vapour phase considers inflow, outflow, droplet evaporation and particle drying:

$$\dot{m}_g \frac{dY_i}{dt} = Y_{in,i}\dot{m}_{in,g} - Y_{out,i}\dot{m}_{out,g} + \dot{m}_{evap,i} + \dot{m}_{drying,i} \tag{61}$$

The energy balance for the vapour phase depends on in flow and outflow of all components as well as particle drying, droplet evaporation, heat transfer to the particles and through the walls into the environment:

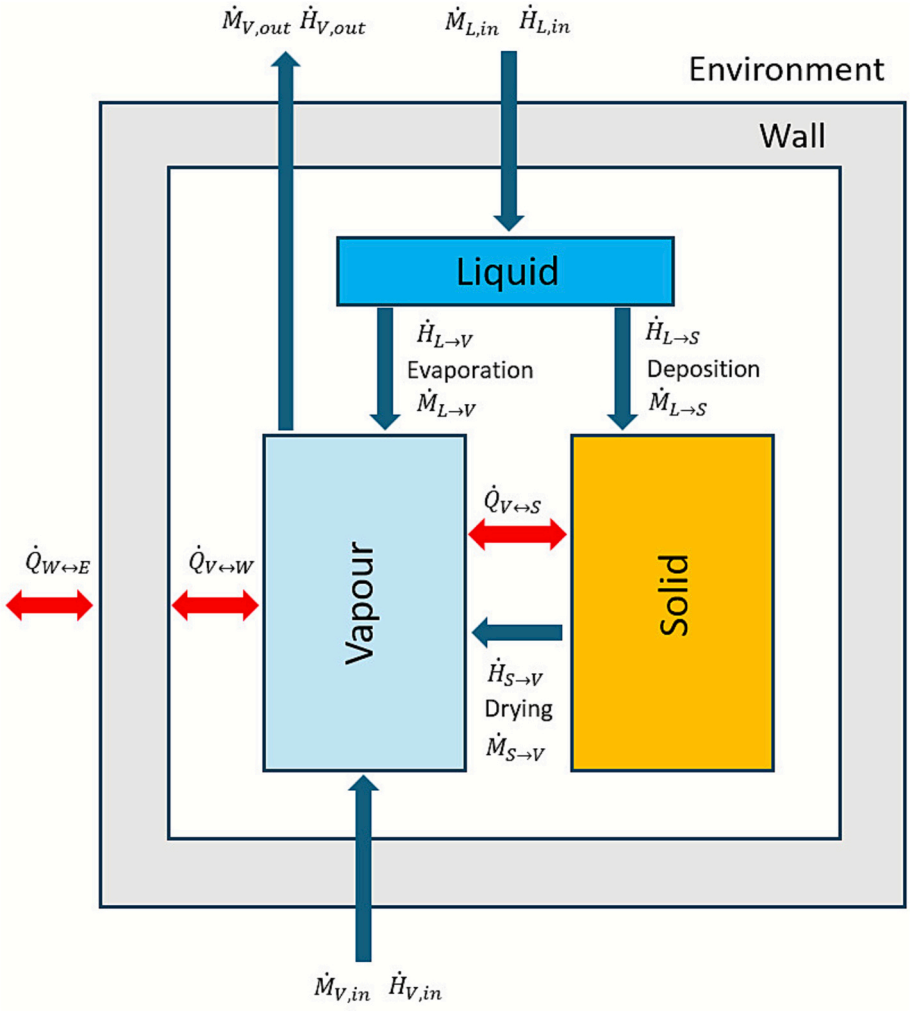

Fig. 9. Scheme of the fluidized bed model setup.

$$\frac{dH_V}{dt} = \dot{H}_{in,g} - \dot{H}_{out,g} - \dot{Q}_{V\leftrightarrow E} - \dot{Q}_{V\leftrightarrow S} + \sum_{i}^{components} \dot{H}_{in,i} - \dot{H}_{out,i} + \dot{H}_{drying,i} + \dot{H}_{evap,i} \tag{62}$$

The accumulated vapour enthalpy H_v depends on the inert gas enthalpy and the enthalpy of evaporated components:

$$H_V = \dot{m}_g \left(cp_g T_V + \sum_{i}^{components} Y_i \left(cp_i T_V + \Delta h_{evap,i} \right) \right) \tag{63}$$

Liquid addition to the system is simplified by not considering droplet atomization and assuming a fixed droplet size instead of a distribution. In literature, the liquid is often distributed independent of particle size. In this study however, an improved particle wetting model is applied, which is described in chapter 3.2.1.1:

$$\dot{m}_{deposition,i} = \frac{\tau_i d_i^2}{\sum_i \tau_i d_i^2} \left(\dot{m}_{L,in} - \dot{m}_{evap,i} \right) \tag{64}$$

The enthalpy flow due to the liquid addition is:

$$\dot{H}_{deposition,i} = cp_i T_{spray} \dot{m}_{deposition,i} \tag{65}$$

Droplets evaporate before deposition on the particle. Evaporation rate $\dot{m}_{evap,i}$ is determined with a lumped evaporation model with the evaporation coefficient k_{evap}, droplet surface area A, species concentration in equilibrium $Y_{eq,i}$ and bulk $Y_{bulk,i}$:

$$\dot{m}_{evap,i} = k_{evap} A_{drop} \left(Y_{eq,i} - Y_{bulk,i} \right) \tag{66}$$

The enthalpy flow due to droplet evaporation is defined as:

$$\dot{H}_{evap,i} = \dot{m}_{evap,i} \left(cp_i \left(T_V - T_{spray} \right) + \Delta h_{evap,i} \right) \tag{67}$$

The equilibrium species concentration in the vapour phase is treated as ideal gas:

$$Y_{eq,i} = \frac{MW_i}{MW_g} \left(\frac{p_{sat,i}}{p - p_{sat,i}} \right) \tag{68}$$

The saturation vapour pressure of water is determined with the Antoine equation:

$$\ln\left(p_{sat,w} \right) = A - \left(\frac{B}{C + T} \right) \tag{69}$$

The drying model used in the simulations is from [70]:

$$\dot{m}_{drying,i} = \nu_i A_i j_i \tag{70}$$

The enthalpy flow from the solid to the vapour phase due to drying is:

$$\dot{H}_{drying,i} = \dot{m}_{drying,i} \left(cp_i \left(T_V - T_S \right) + \Delta h_{evap,i} \right) \tag{71}$$

The mass flux is calculated according to [70]:

$$j_i = \rho_g k_{drying,i} \left(Y_{eq,i} - Y_{bulk,i} \right) \tag{72}$$

The mass transfer coefficient $k_{drying,i}$ is calculated according to [70].

The critical moisture content is used as a fitting parameter while the bulk Sherwood number correction factor is not adjusted:

$$k_{drying,i} = \frac{Sh_{bulk,i} D_i}{d_i} \tag{73}$$

The bulk Sherwood number is defined by scaling the single particle dimensionless number and correcting with the bulk Sherwood number correction factor ϵ:

$$Sh_{bulk,i} = \frac{\epsilon Re_0 Sc_i}{\frac{A_i}{A_{inlet}}} ln\left(1 + \frac{Sh_i \frac{A_p}{A_{inlet}}}{Re_0 Sc_i}\right) \tag{74}$$

The Sherwood number for a single particle is defined according to [71]:

$$Sh_i = 2 + 0.6 Re_0^{\frac{1}{2}} Sc_i^{\frac{1}{3}} \tag{75}$$

The Reynolds number at superficial gas velocity is as follows:

$$Re_0 = \frac{u_0\, d_i}{\nu_0} \tag{76}$$

The superficial gas velocity is then:

$$u_0 = \frac{\dot{V}_g}{A_{inlet}} \tag{77}$$

The Schmidt number is defined as:

$$Sc_i = \frac{\mu_g}{\rho_g D_i} \tag{78}$$

The drying curve is a linear single particle drying curve:

$$\nu_i = \begin{cases} \eta_i, & \eta_i < 1 \\ 1, & \eta_i > 1 \end{cases} \tag{79}$$

The relative moisture content is defined as:

$$\eta_i = \frac{X_i - X_{eq,i}}{X_{cr,i} - X_{eq,i}} \tag{80}$$

The sorption isotherm is modelled with the Brunauer-Emmett-Teller theory [72] as the sorption isotherm is almost temperature independent. The BET coefficients are taken from [55]:

$$X_{eq,i} = m_m \frac{n\alpha_i}{(1-\alpha_i)(1+(n-1)\alpha_i)} \tag{81}$$

The water activity equals the fraction of vapour pressure and saturation vapour pressure:

$$\alpha_i = \frac{p_i}{p_{sat,i}} \tag{82}$$

The vapour pressure depends on the species volume fraction and the total pressure:

$$p_i = y_i p \tag{83}$$

The heat loss over the reactor wall is calculated with a fitted constant heat transfer coefficient:

$$\dot{Q}_{V \leftrightarrow E} = k_{wall} A_{wall} (T_V - T_{env}) \tag{84}$$

The heat transfer rate between the solid and vapour phase is calculated according to [70]:

$$\dot{Q}_{V \leftrightarrow S} = h_c A_i (T_V - T_S) \tag{85}$$

The heat transfer coefficient is dependent on the bulk Nusselt number Nu_{bulk}, the thermal conductivity λ_g and the particle diameter d_i:

$$h_c = \frac{Nu_{bulk} \lambda_g}{d_i} \tag{86}$$

The bulk Nusselt number derives from correlations of the single particle dimensionless numbers:

$$Nu_{bulk} = \frac{Re_0 Pr}{\frac{A_p}{A_{inlet}}} ln\left(1 + \frac{Nu \frac{A_p}{A_{inlet}}}{Re_0 Pr}\right) \tag{87}$$

The single particle Nusselt number is defined according to [71]:

$$Nu = 2 + 0.6 Re_0^{\frac{1}{2}} Pr^{\frac{1}{3}} \tag{88}$$

The Prandtl number is defined by the specific heat capacity, dynamic viscosity and thermal conductivity:

$$Pr = \frac{Cp_g \mu_g}{\lambda_g} \tag{89}$$

The model parameters and coefficients are collected in Table 8.

The parameters for the agglomeration rate including the glass transition success factor is described in chapter 3.2.2.1. The settings are displayed in Table 9.

Breakage is determined according to [73]. The breakage rate is a function of the breakage rate constant k'_{break}, material parameter f_{Mat}, particle size d_i, mass based kinetic impact energy causing breakage $E_{m,kin}$ and the mass based threshold energy $E_{m,min}$:

$$K_{break}(d) = k'_{break}\left(1 - \exp\left(-f_{Mat} d_i \left(E_{m,kin} - E_{m,min}\right)\right)\right) \tag{90}$$

The kinetic impact energy is defined via particle size d_i, minimum diameter for breakage $d_{min,break}$ and the threshold energy $E_{m,min}$:

$$E_{m,kin} = \frac{d_i E_{m,min}}{d_{min,break}} \tag{91}$$

Leading to an alternate version with a lumped term $f_{Mat} E_{m,min}$ and minimum diameter for breakage $d_{min,break}$ which are both set to default values:

$$K_{break}(d) = k'_{break}\left(1 - \exp\left(-f_{Mat} E_{m,min} d_i \left(\frac{d_i}{d_{min,break}} - 1\right)\right)\right) \tag{92}$$

The cumulative fragment size distribution b_{cum} is determined according to [74]. q represents the power law exponent and $d_{j,min}$ the minimum fragment size:

$$b_{cum}(d_i, d_j) = \left(\frac{d_i}{d_j}\right)^q \frac{1}{2}\left(1 + tanh\left(\frac{d_j - d_{j,min}}{d_{j,min}}\right)\right) \tag{93}$$

The coefficients are shown in Table 10.

The model framework needs to be calibrated in multiple steps to improve convergence. First, the heat and mass transfer are calibrated. The size then follows and then all parameters are calibrated simultaneously as shown in Fig. 10.

Table 8
Heat- and mass transfer model parameters.

Parameter	Unit	Value
Heat loss		
Wall heat transfer coefficient	W m^{-2} °C^{-1}	13.8
Wetting		
Coefficient 1		-3e-3
Intercept		0.23
Evaporation		
Evaporation coefficient		3e-3
Drying		
Critical moisture content	kg kg_{dry}^{-1}	0.07
Bulk Sherwood number correction	–	1
BET m_m at 20 °C	wt%	3.7
BET n at 20 °C	–	11.9
Antoine A		16.262
Antoine B		3800
Antoine C		226.3

Table 9
Agglomeration parameters including the glass transition success factor kernel.

Parameter	Unit	Value
Agglomeration rate constant	ln(1/s)	−17.24
Droplet diameter	μm	30
Sticky offset	°C	20
Linear slope glass transition		8.733
Glass transition constant		6.4
Glass transition temperature liquid	°C	−135
Glass transition temperature liquid	°C	167
Spray zone diameter	m	0.3
Coefficient 1 solid mass fraction Reynolds number		-3e-4
Coefficient 2 solid mass fraction Reynolds number		5.5e-3
Coefficient 3 solid mass fraction intercept		0.13
Coefficient 1 particle velocity Reynolds number		1.0e-2
Coefficient 2 particle velocity fraction intercept		6.6e-2
Penetration depth	μm	168
Liquid density	$kg\ m^{-3}$	1000
Particle density	$kg\,m^{-3}$	900
Dimensionless mean residence time	–	0.22

Table 10
Breakage parameters.

Parameter	Unit	Value
Breakage		
Breakage rate constant	s^{-1}	1.3e-3
Minimum breakage diameter	μm	50
Material parameter	–	1
Minimum threshold breakage energy	J	0.3
Fragmentation		
Power law exponent	–	0.5
Minimum particle size	μm	50

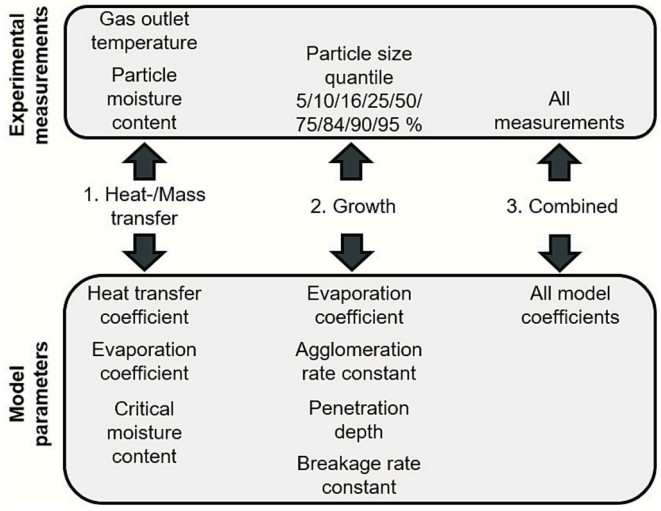

Fig. 10. PBM calibration workflow displaying experimental measurements (top), calibrated mechanism (center) and model coefficients (bottom).

4. Results and discussion

This chapter discusses the accuracy of the PBM framework, the impact of the glass transition success factor and the surrogate models on the prediction.

The kernel performance in capturing the complex physics of particle agglomeration in fluidized beds is demonstrated by comparative analysis. This section focuses on validating the presented PBM using experimental data, focusing on its significance in improving the accuracy of mechanistic agglomeration process modelling.

Contour plots demonstrate the impact of the process and model parameters on agglomeration. An exemplary design-space exploration is executed to determine suitable process parameters for a chosen product.

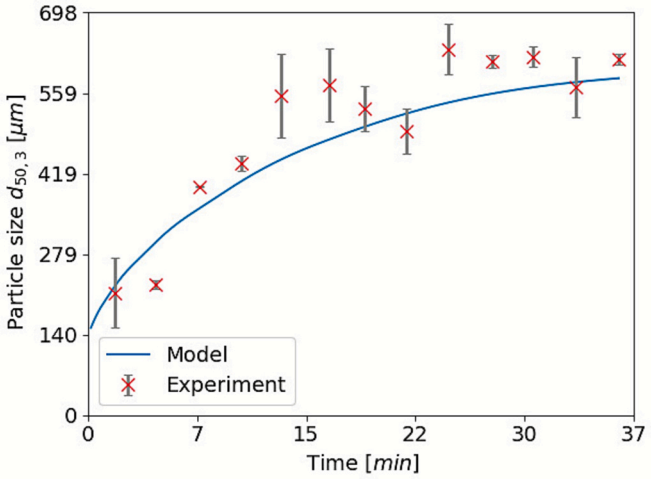

Fig. 11. Evolution of particle size ($d_{50,3}$) over time for run B009 at inlet air temperature 80 °C, inlet air flow rate 600 $m^3\ h^{-1}$ and spray water mass flow rate 120 g min^{-1}.

4.1. Fluidized bed agglomeration analysis

This chapter analyses the agglomeration of maltodextrin using the proposed model framework and displays the influence of model parameters and process parameters.

As shown in Fig. 11, particle size increases over time and approaches equilibrium after approximately 25 min. The model reproduces the overall growth trend, but the simulated equilibrium is reached earlier than observed experimentally. While the equilibrium size ($d_{50,3}$) is predicted accurately, $d_{90,3}$ is underestimated and $d_{10,3}$ is overestimated, indicating that the model captures the mean size but struggles to reproduce the evolution of the size-distribution width. In all three metrics ($d_{10,3}$, $d_{50,3}$, $d_{90,3}$), particle growth proceeds more rapidly in the simulation before slowing sharply, which explains the earlier approach to equilibrium in the model.

Overall, the particle size can be predicted with an R^2 of 0.72 on the calibration dataset and 0.67 on the validation dataset. The small difference in R^2 between calibration and validation data shows that there is

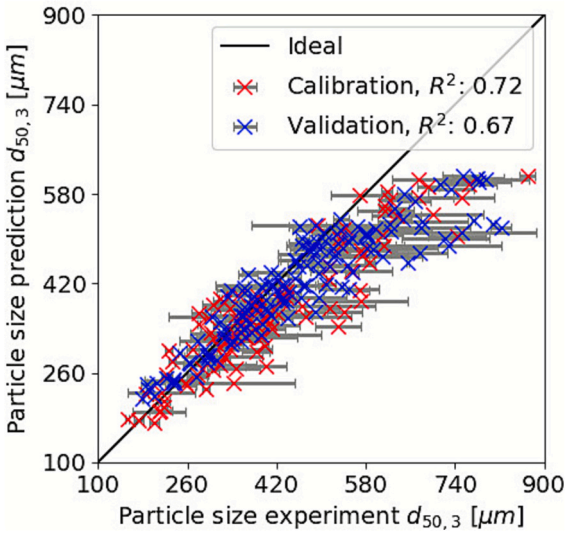

Fig. 12. Particle size parity plot for all samples.

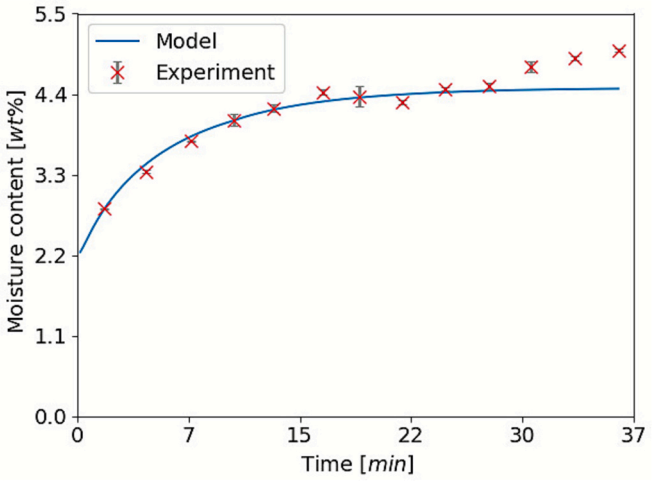

Fig. 13. Particle moisture evolution over time of B009 at an inlet air temperature of 80 °C, inlet air flow rate of 600 $m^3\ h^{-1}$ and a spray water mass flow rate of 120 g min^{-1}.

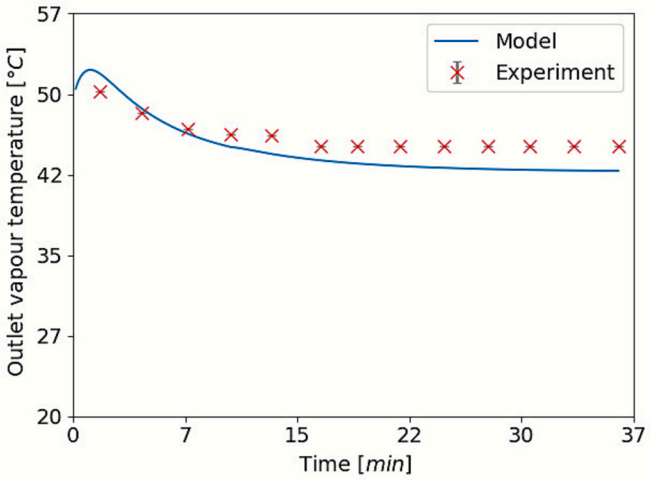

Fig. 15. Gas outlet temperature evolution over time of B009 at an inlet air temperature of 80 °C, inlet air flow rate of 600 $m^3\ h^{-1}$ and a spray water mass flow rate of 120 g min^{-1}.

no overfitting and the model generalizes well. The experimental standard deviation is on average 7.2 % for the $d_{50,3}$ and the model predicts in the range of the experimental standard deviation. As shown in Fig. 12, lower particle sizes are better predicted than large particle sizes. This is due to the loss function used in the solver. In this study, relative variances are used to avoid putting too much weight on low values when minimizing the loss function. When the model framework is calibrated without breakage the larger particles are better predicted. However, the smaller particles are poorly represented, which ultimately leads to a better prediction of equilibrium size but a worse prediction of particle growth dynamics.

Upon initiation of spraying, particle-bed moisture content rises and stabilizes after roughly 15 min (Fig. 13). The model reproduces the heat- and mass-transfer-driven moisture evolution well.

Notably, Fig. 11 reveals that particle size equilibrium is achieved considerably later than moisture equilibrium. In the simulations, slow size growth continues after moisture stabilization, suggesting that most agglomeration occurs primarily within the spray zone.

Since it is not possible to take samples inside the spray zone, samples that are taken from experiments only reflect the average moisture content.

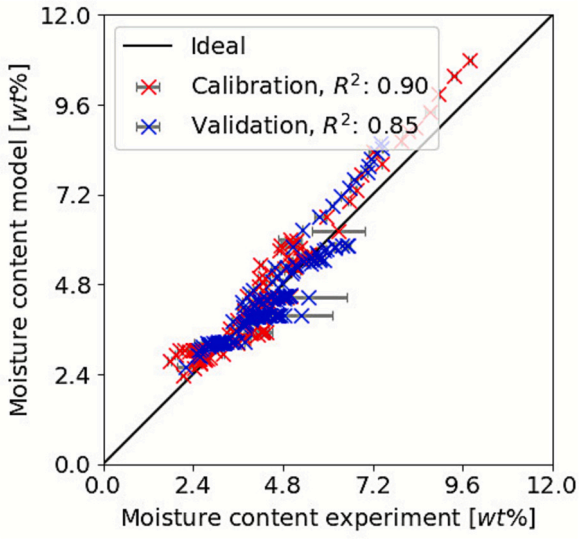

Fig. 14. Particle moisture parity plot for all samples.

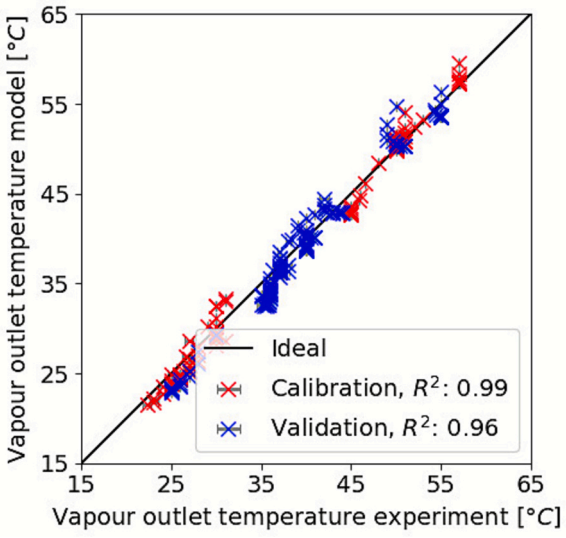

Fig. 16. Vapour outlet temperature parity plot for all samples.

The moisture content is well predicted with an R^2 of 0.9 on the calibration dataset and 0.85 on the validation dataset (Fig. 14). The model does not show the same moisture content range as the experiments in multiple cases with lower moisture contents. In multiple cases the moisture content equilibrium is reached faster than in experiments. Overall, the trends of all the experiments are correctly captured.

The vapour outlet temperature profile over time is well captured in the model (Fig. 15). The trends over time and for different process parameters are correct.

The gas outlet temperature is captured well with an R^2 of 0.99 on the calibration data and 0.96 on the validation data. From Fig. 16 it can be seen that lower vapour outlet temperatures tend to be underestimated while higher temperatures are overestimated.

It is not unexpected that the particle size prediction has the highest error while the vapour outlet temperature has the lowest. This is due to the severe dependence of the particle size on the moisture content and temperature. The moisture content and vapour temperature rely on less calibration parameters because of a weaker dependence on other parameters.

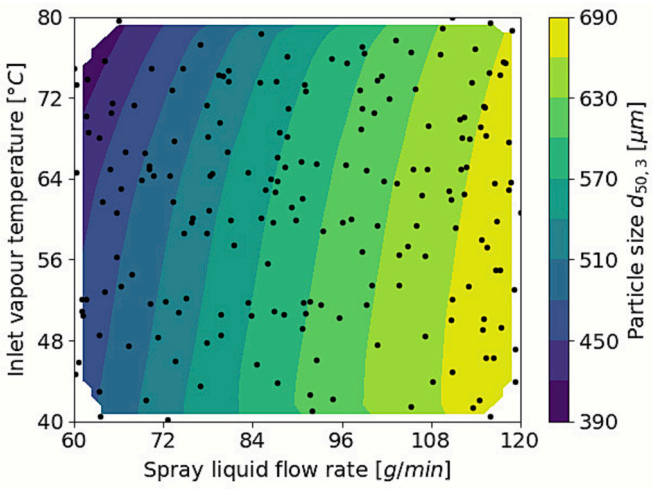

Fig. 17. Particle size after 60min as a function of inlet air temperature and spray mass flow rate.

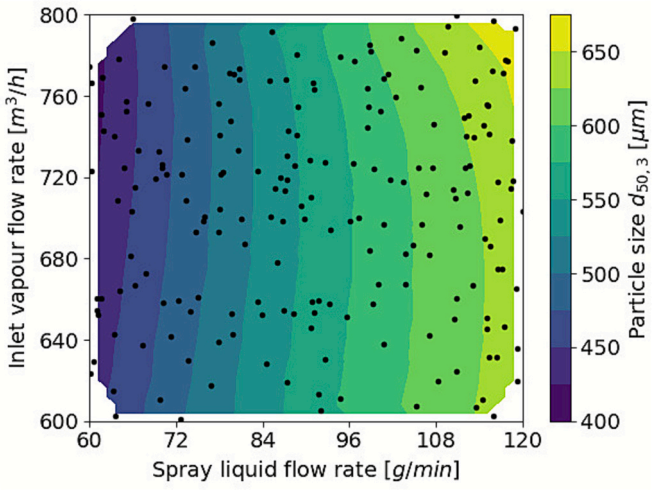

Fig. 18. Particle size after 60 min as a function of inlet air volume flow rate and spray mass flow rate.

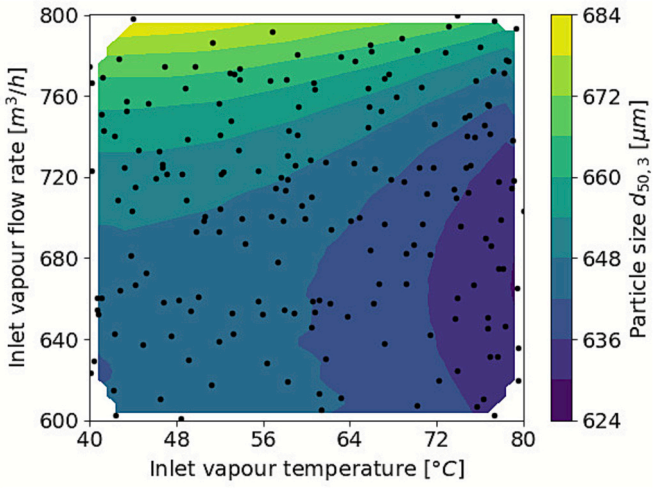

Fig. 19. Particle size after 60 min as a function of inlet air temperature and inlet air volume flow.

4.2. Influence of process parameters

The effects of the process parameters on intrinsic process conditions can be visualized with a contour plot, as outlined in Fig. 17. This allows one to choose optimal operating conditions. The figures are shown exemplary for the center case with parameters 700 $m^3\ h^{-1}$ inlet air flow rate, 60°C inlet air temperature and 90 $g\ min^{-1}$ spray water flow rate. The following figures show the d_{50} after 60min of operation.

The particle size increases with spray mass flow rate and decreases with inlet vapour temperature. The equilibrium agglomerate size can be estimated from Fig. 17. From the slopes of the contour lines it is clearly visible that the spray liquid flow rate has a higher impact on the particle size than the inlet vapour temperature.

In Fig. 18 it can be seen that the spray liquid flow rate has a higher impact than the inlet vapour flow rate.

In Fig. 19 inlet vapour temperature and inlet vapour flow rate show a similar impact on the particle size.

Fig. 19 is clearly less impactful as the range in particle size is lower. Both show a similar impact on the granule size while the spray flow rate has the highest influence on the particle size.

4.3. Design-space exploration

Design-space exploration is used to find appropriate process parameters for predefined product properties such as a minimum size, narrow, or wide size distribution. Design space exploration can not only be applied to product properties but it can also be used to avoid the need for a following drying step in additional equipment. In the pharmaceutical industry, temperature sensitivity of ingredients makes a temperature limitation necessary.

The design-space exploration incorporated in gProms allows, one to explore suitable process conditions such as, the spray water mass flow rate and the inlet air temperature shown exemplary in Fig. 20. The design-space exploration allows to predict the conditions in the process chamber at different times and process parameters using a calibrated PBM model. The limitations set for Fig. 20 include a minimum product size ($d_{50,3}$) of 400 μm and a moisture content below 4 %. The experimental parameters marked in red are the ones that produce particles with the chosen product properties.

4.4. Wetting model analysis

The surrogate models developed for predicting particle wetting and velocity demonstrated acceptable predictive accuracy across a range of

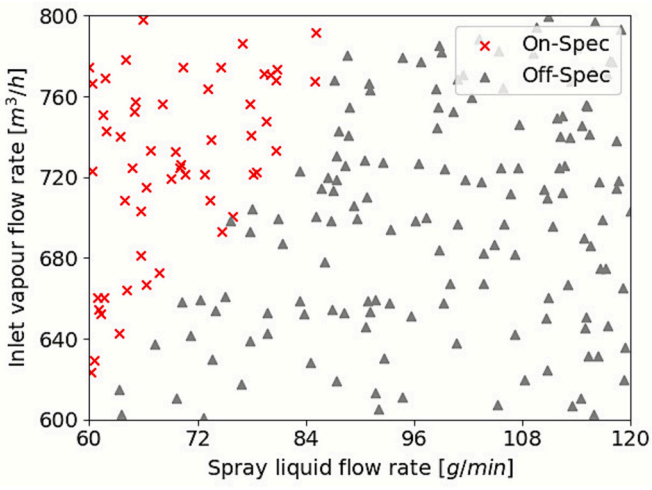

Fig. 20. Design-space exploration to reach predefined product properties of a $d_{50,3}$ above 400 μm and a moisture content below 4 wt% after 60 min.

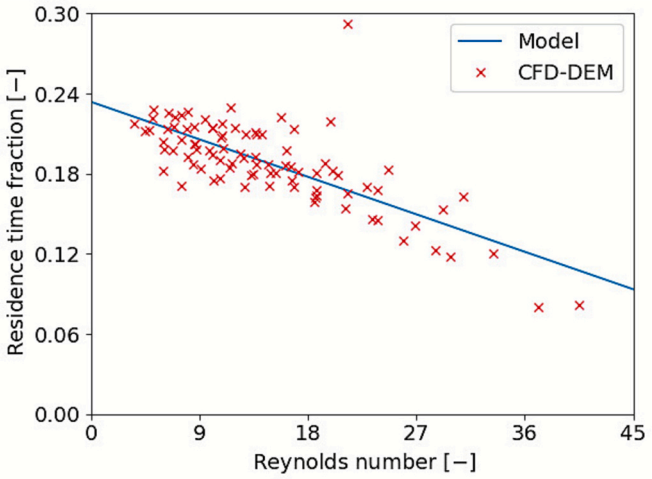

Fig. 21. Predicted dimensionless residence time fraction over Reynolds number.

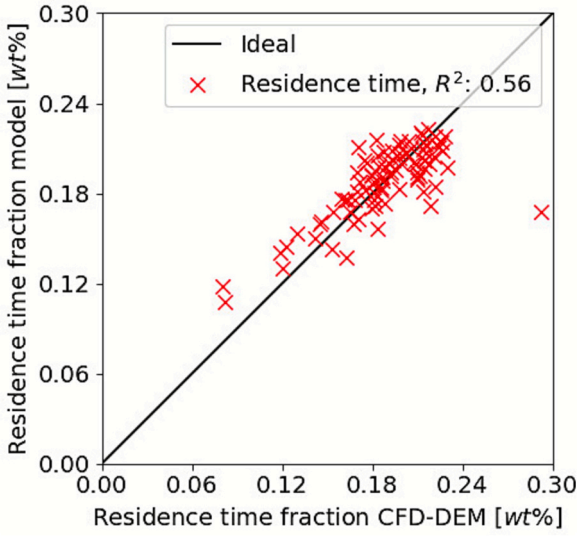

Fig. 22. Parity plot showing the predicted dimensionless residence time compared to the dimensionless residence time from CFD-DEM simulations.

operational conditions in fluidized beds. This section provides an overview of the model's performance, highlighting the capability of CFD-DEM in capturing the complex interactions between particles and fluid dynamics in fluidized beds. A detailed introduction to the model can be found in 3.2.1.1. The residence time determines the time a particle spends in the spray zone. This is an indication of the exposure of a particle to the spray and the liquid droplets. The residence time is influenced by many factors such as the bed mass, particles size and inlet air velocity. The overall trend can be well captured with the Reynolds number, as shown in Fig. 21.

The model developed in chapter 3.2.1.1 fits with an R^2 of 56 %. Fig. 22 shows the parity plot for the model prediction.

5. Conclusion

This study introduces, a novel computationally efficient framework for deploying PBM to predict the agglomeration behavior of amorphous substances in fluidized beds. A new agglomeration kernel based on the glass-transition criterion integrates material properties with process conditions, enabling the modelling of both sintering and non-binder based agglomeration mechanisms via coupled mass and energy balance relations. The PBM framework reproduces agglomeration with satisfactory accuracy and physically consistent trends across all process parameters. The prediction accuracies for particle size, particle moisture content and vapour outlet temperature were quantified with R^2-values of 72 %, 90 % and 99 % for the calibration dataset and 67 %, 85 % and 96 % for the unseen validation dataset. The slightly lower performance on the validation data indicates that the model does not overfit.

The incorporation of CFD-DEM-derived surrogate models into PBM simulations allows consideration of additional physical aspects while maintaining computational feasibility. This method expands the predictive power of PBM models by considering the influence of geometry on the process, provides critical information where experiments fail and shows a practical utilization for large-scale industrial simulations.

The process-parameter analysis revealed that the liquid-spray flow rate exerts the strongest influence on particle growth, compared with the inlet gas flow rate and temperature

Design-space exploration enables the identification of suitable process-parameter windows for a given product specification.

Beyond the present study, several directions for future work emerge. First, applying the proposed framework to other maltodextrins, glucose syrups and other amorphous materials with composition-dependent glass transition temperatures would help assess the generality of the glass-transition-based success factor. Second, dedicated experiments to directly measure sticking probabilities in single particle collision setup would provide additional validation and parameterization data. Third, developing more mechanistic descriptions of attrition and breakage could improve the prediction of particle size distribution width and tails for brittle agglomerates. Finally, extending the DEM-informed closure correlations or replacing them with data-driven closures trained on larger datasets, offers a route to further refine the wetting models while keeping the overall framework computationally efficient.

CRediT authorship contribution statement

Gero Stoeckl: Writing – review & editing, Writing – original draft, Visualization, Validation, Methodology, Investigation, Formal analysis, Data curation, Conceptualization. **Stefan Bellinghausen:** Writing – review & editing, Supervision, Software, Resources, Methodology. **Stefan Heinrich:** Writing – review & editing, Project administration, Funding acquisition.

Declaration of competing interest

The authors declare the following financial interests/personal relationships which may be considered as potential competing interests: Stefan Bellinghausen works for Siemens AG and is actively involved in developing and commercially supporting the software platform gPROMS used in this work. The other authors declare that they have no known competing financial interests or personal relationships that could have appeared to influence the work reported in this paper.

Data availability

The experimental and simulation data can be found here: https://doi.org/10.15480/882.15266.

Acknowledgements

This project has received funding from the European Union's Horizon 2020 research and innovation programme under the Marie Skłodowska Curie grant agreement No 955661.

The authors would like to thank Marie Schellenberg from Hamburg University of Technology for the contributions during the experiments on the lab scale device. The authors would like to thank Jhoan Giraldo Yepes from Hamburg University of Technology for the contributions during the experiments on the pilot scale device.

References

[1] S. Heinrich, M. Peglow, M. Ihlow, L. Mörl, Particle population modeling in fluidized bed-spray granulation—analysis of the steady state and unsteady behavior, Powder Technol. 130 (1–3) (2003) 154–161, https://doi.org/10.1016/S0032-5910(02)00259-0.

[2] B. Wang, H. Li, J. Xiang, J. Zheng, J. Wang, Fabrication of agglomerated lactose using fluidized bed for good compressibility, J. Nanomater. 2021 (2021) 1–6, https://doi.org/10.1155/2021/9918847.

[3] H. Yuksel, N. Dirim, Agglomeration process in the fluidized bed, the effecting parameters and some applications, Hrvatski Časopis Za Prehrambenu Tehnologiju, Biotehnologiju i Nutricionizam 13 (3–4) (2018) 159–163, https://doi.org/10.31895/hcptbn.13.3-4.10.

[4] S. Shanmugam, Granulation techniques and technologies: recent progresses, BioImpacts 5 (1) (2017) 55–63, https://doi.org/10.15171/bi.2015.04.

[5] A.A. Ouazzou, Y.M. Harshe, V. Meunier, J.H. Finke, S. Heinrich, Influence of process parameters and particle size distribution on mechanical properties of tablets, Chemie-Ingenieur-Technik 95 (1–2) (2023) 168–177, https://doi.org/10.1002/cite.202200157.

[6] B. Rambali, L. Baert, D.L. Massart, Using experimental design to optimize the process parameters in fluidized bed granulation on a semi-full scale, Int. J. Pharm. 220 (1–2) (2001) 149–160, https://doi.org/10.1016/S0378-5173(01)00658-5.

[7] C. Avilés-Avilés, E. Dumoulin, C. Turchiuli, Fluidised bed agglomeration of particles with different glass transition temperatures, Powder Technol. 270 (2015) 445–452, https://doi.org/10.1016/j.powtec.2014.03.026.

[8] M. Askarishahi, M. Salehi, S. Radl, Full-physics simulations of spray-particle interaction in a bubbling fluidized bed, AIChE J. 63 (7) (2017) 2569–2587, https://doi.org/10.1002/aic.15616.

[9] M. Askarishahi, M.-S. Salehi, M. Maus, D. Schröder, D. Slade, D. Jajcevic, Mechanistic modelling of fluid bed granulation, part II: eased process development via degree of wetness, Int. J. Pharm. 572 (2019) 118836, https://doi.org/10.1016/j.ijpharm.2019.118836.

[10] M. Askarishahi, M.-S. Salehi, S. Radl, Two-fluid-model-based full physics simulations of mixing in noncohesive wet fluidized beds, Ind. Eng. Chem. Res. 58 (27) (2019) 12323–12346, https://doi.org/10.1021/acs.iecr.9b01344.

[11] K. Terrazas-Velarde, M. Peglow, E. Tsotsas, Kinetics of fluidized bed spray agglomeration for compact and porous particles, Chem. Eng. Sci. 66 (9) (2011) 1866–1878, https://doi.org/10.1016/j.ces.2011.01.037.

[12] J. Tausendschön, S. Radl, Deep neural network-based heat radiation modelling between particles and between walls and particles, Int. J. Heat Mass Transf. 177 (2021) 121557, https://doi.org/10.1016/j.ijheatmasstransfer.2021.121557.

[13] J. Tausendschön, G. Stöckl, S. Radl, Machine learning for heat radiation modeling of bi- and polydisperse particle systems including walls, Particuology 74 (2023) 119–140, https://doi.org/10.1016/j.partic.2022.05.011.

[14] C. Zheng, L. Zhang, N. Govender, C.Y. Wu, DEM analysis of residence time distribution during twin screw granulation, Powder Technol. 377 (2021) 924–938, https://doi.org/10.1016/J.POWTEC.2020.09.049.

[15] D. Barrasso, R. Ramachandran, Qualitative assessment of a multi-scale, compartmental PBM-DEM model of a continuous twin-screw wet granulation process, J. Pharm. Innov. 11 (3) (2016) 231–249, https://doi.org/10.1007/S12247-015-9240-7/METRICS.

[16] Z. Peng, E. Doroodchi, G. Evans, DEM simulation of aggregation of suspended nanoparticles, Powder Technol. 204 (1) (2010) 91–102, https://doi.org/10.1016/J.POWTEC.2010.07.023.

[17] A. Atxutegi, P. Kieckhefen, S. Pietsch, R. Aguado, M. Olazar, S. Heinrich, Unresolved CFD-DEM simulation of spherical and ellipsoidal particles in conical and prismatic spouted beds, Powder Technol. 389 (2021) 493–506, https://doi.org/10.1016/j.powtec.2021.05.012.

[18] E. Diez, P. Kieckhefen, K. Meyer, A. Bück, E. Tsotsas, S. Heinrich, Particle dynamics in a multi-staged fluidized bed: particle transport behavior on micro-scale by discrete particle modelling, Adv. Powder Technol. 30 (10) (2019) 2014–2031, https://doi.org/10.1016/j.apt.2019.05.025.

[19] L. Fries, S. Antonyuk, S. Heinrich, S. Palzer, DEM–CFD modeling of a fluidized bed spray granulator, Chem. Eng. Sci. 66 (11) (2011) 2340–2355, https://doi.org/10.1016/J.CES.2011.02.038.

[20] L. Fries, M. Dosta, S. Antonyuk, S. Heinrich, S. Palzer, Moisture distribution in fluidized beds with liquid injection, Chem. Eng. Technol. 34 (7) (2011) 1076–1084, https://doi.org/10.1002/ceat.201100132.

[21] P. Kieckhefen, T. Lichtenegger, S. Pietsch, S. Pirker, S. Heinrich, Simulation of spray coating in a spouted bed using recurrence CFD, Particuology 42 (2019) 92–103, https://doi.org/10.1016/j.partic.2018.01.008.

[22] P. Kieckhefen, S. Pietsch, M. Dosta, S. Heinrich, Possibilities and limits of computational fluid dynamics–discrete element method simulations in process engineering: a review of recent advancements and future trends, Annu. Rev. Chem. Biomol. Eng. 11 (1) (2020) 397–422, https://doi.org/10.1146/annurev-chembioeng-110519-075414.

[23] P. Kieckhefen, S. Pietsch, M. Höfert, M. Schönherr, S. Heinrich, F. Kleine Jäger, Influence of gas inflow modelling on CFD-DEM simulations of three-dimensional prismatic spouted beds, Powder Technol. 329 (2018) 167–180, https://doi.org/10.1016/j.powtec.2018.01.048.

[24] T. Lichtenegger, P. Kieckhefen, S. Heinrich, S. Pirker, Dynamics and long-time behavior of gas–solid flows on recurrent-transient backgrounds, Chem. Eng. J. 364 (2019) 562–577, https://doi.org/10.1016/j.cej.2019.01.161.

[25] S. Pietsch, P. Kieckhefen, S. Heinrich, M. Müller, M. Schönherr, F. Kleine Jäger, CFD-DEM modelling of circulation frequencies and residence times in a prismatic spouted bed, Chem. Eng. Res. Des. 132 (2018) 1105–1116, https://doi.org/10.1016/j.cherd.2018.01.013.

[26] S. Pietsch, P. Kieckhefen, M. Müller, M. Schönherr, F. Kleine Jäger, S. Heinrich, Influence of binary and ternary particle systems on the spouting stability in a three-dimensional prismatic spouted bed, Powder Technol. 357 (2019) 305–312, https://doi.org/10.1016/j.powtec.2019.08.065.

[27] M. Wu, J.G. Khinast, S. Radl, The effect of liquid bridge model details on the dynamics of wet fluidized beds, AICHE J. 64 (2) (2018) 437–456, https://doi.org/10.1002/aic.15947.

[28] A. Ding, M.J. Hounslow, C.A. Biggs, Population balance modelling of activated sludge flocculation: investigating the size dependence of aggregation, breakage and collision efficiency, Chem. Eng. Sci. 61 (1) (2006) 63–74, https://doi.org/10.1016/J.CES.2005.02.074.

[29] M. Hussain, J. Kumar, M. Peglow, E. Tsotsas, Modeling spray fluidized bed aggregation kinetics on the basis of Monte-Carlo simulation results, Chem. Eng. Sci. 101 (2013) 35–45, https://doi.org/10.1016/J.CES.2013.06.004.

[30] J.A. Gantt, I.T. Cameron, J.D. Litster, E.P. Gatzke, Determination of coalescence kernels for high-shear granulation using DEM simulations, Powder Technol. 170 (2) (2006) 53–63, https://doi.org/10.1016/J.POWTEC.2006.08.002.

[31] A. Reinhold, H. Briesen, Numerical behavior of a multiscale aggregation model—coupling population balances and discrete element models, Chem. Eng. Sci. 70 (2012) 165–175, https://doi.org/10.1016/J.CES.2011.06.041.

[32] B. Freireich, J. Li, J. Litster, C. Wassgren, Incorporating particle flow information from discrete element simulations in population balance models of mixer-coaters, Chem. Eng. Sci. 66 (16) (2011) 3592–3604, https://doi.org/10.1016/j.ces.2011.04.015.

[33] J. Li, B.J. Freireich, C.R. Wassgren, J.D. Litster, Experimental validation of a 2-D population balance model for spray coating processes, Chem. Eng. Sci. 95 (2013) 360–365, https://doi.org/10.1016/j.ces.2012.02.036.

[34] M. Sen, A. Dubey, R. Singh, R. Ramachandran, Mathematical development and comparison of a hybrid PBM-DEM description of a continuous powder mixing process, J. Powder Technol. 2013 (2013) 1–11, https://doi.org/10.1155/2013/843784.

[35] M. Dosta, T.T. Chan, Linking process-property relationships for multicomponent agglomerates using DEM-ANN-PBM coupling, Powder Technol. 398 (2022) 117156, https://doi.org/10.1016/J.POWTEC.2022.117156.

[36] M. Capece, R.N. Davé, E. Bilgili, A pseudo-coupled DEM–non-linear PBM approach for simulating the evolution of particle size during dry milling, Powder Technol. 323 (2018) 374–384, https://doi.org/10.1016/J.POWTEC.2017.10.008.

[37] D. Barrasso, T. Eppinger, F.E. Pereira, R. Aglave, K. Debus, S.K. Bermingham, R. Ramachandran, A multi-scale, mechanistic model of a wet granulation process using a novel bi-directional PBM–DEM coupling algorithm, Chem. Eng. Sci. 123 (2015) 500–513, https://doi.org/10.1016/J.CES.2014.11.011.

[38] D. Barrasso, R. Ramachandran, Multi-scale modeling of granulation processes: bi-directional coupling of PBM with DEM via collision frequencies, Chem. Eng. Res. Des. 93 (2015) 304–317, https://doi.org/10.1016/J.CHERD.2014.04.016.

[39] D. Barrasso, A. Tamrakar, R. Ramachandran, A reduced order PBM–ANN model of a multi-scale PBM–DEM description of a wet granulation process, Chem. Eng. Sci. 119 (2014) 319–329, https://doi.org/10.1016/J.CES.2014.08.005.

[40] M. Sen, D. Barrasso, R. Singh, R. Ramachandran, A multi-scale hybrid CFD-DEM-PBM description of a fluid-bed granulation process, Processes 2 (1) (2014) 89–111, https://doi.org/10.3390/PR2010089.

[41] M. Sen, R. Ramachandran, A multi-dimensional population balance model approach to continuous powder mixing processes, Adv. Powder Technol. 24 (1) (2013) 51–59, https://doi.org/10.1016/J.APT.2012.02.001.

[42] A. Tamrakar, R. Ramachandran, CFD–DEM–PBM coupled model development and validation of a 3D top-spray fluidized bed wet granulation process, Comput. Chem. Eng. 125 (2019) 249–270, https://doi.org/10.1016/J.COMPCHEMENG.2019.01.023.

[43] T. Baba, H. Nakamura, H. Takimoto, S. Ohsaki, S. Watano, K. Takehara, T. Higuchi, T. Hirosawa, T. Yamamoto, DEM–PBM coupling method for the layering granulation of iron ore, Powder Technol. 378 (2021) 40–50, https://doi.org/10.1016/J.POWTEC.2020.09.059.

[44] H. Eisenschmidt, M. Soumaya, N. Bajcinca, S. Le Borne, K. Sundmacher, Estimation of aggregation kernels based on Laurent polynomial approximation, Comput. Chem. Eng. 103 (2017) 210–217, https://doi.org/10.1016/j.compchemeng.2017.03.018.

[45] M. Peglow, J. Kumar, L. Mörl, Investigation of coalescence kinetics of microcristalline cellulose in fluidised bed spray agglomeration: experimental studies and modelling approach, Braz. J. Chem. Eng. 22 (2) (2005) 165–172, https://doi.org/10.1590/S0104-66322005000200002.

[46] M. Peglow, J. Kumar, G. Warnecke, S. Heinrich, L. Mörl, A new technique to determine rate constants for growth and agglomeration with size- and time-dependent nuclei formation, Chem. Eng. Sci. 61 (1) (2006) 282–292, https://doi.org/10.1016/j.ces.2004.11.071.
[47] P.C. Kapur, Kinetics of granulation by non-random coalescence mechanism, Chem. Eng. Sci. 27 (10) (1972) 1863–1869, https://doi.org/10.1016/0009-2509(72)85048-6.
[48] M. Askarishahi, M. Maus, D. Schröder, D. Slade, M. Martinetz, D. Jajcevic, Mechanistic modelling of fluid bed granulation, part I: agglomeration in pilot scale process, Int. J. Pharm. 573 (2020) 118837, https://doi.org/10.1016/j.ijpharm.2019.118837.
[49] P. Rajniak, F. Stepanek, K. Dhanasekharan, R. Fan, C. Mancinelli, R.T. Chern, A combined experimental and computational study of wet granulation in a Wurster fluid bed granulator, Powder Technol. 189 (2) (2009) 190–201, https://doi.org/10.1016/j.powtec.2008.04.027.
[50] C. Rieck, M. Schmidt, A. Bück, E. Tsotsas, Monte Carlo modeling of binder-less spray agglomeration in fluidized beds, AIChE J. 64 (10) (2018) 3582–3594, https://doi.org/10.1002/aic.16349.
[51] L. Sperling, Introduction to physical polymer science, Wiley, 1986, pp. 224–295.
[52] D. Ramkrishna, A.W. Mahoney, Population balance modeling. Promise for the future, Chem. Eng. Sci. 57 (4) (2002) 595–606, https://doi.org/10.1016/S0009-2509(01)00386-4.
[53] Hounslow, H.S. Mumtaz, A.P. Collier, J.P. Barrick, A.S. Bramley, A micro-mechanical model for the rate of aggregation during precipitation from solution, Chem. Eng. Sci. 56 (7) (2001) 2543–2552, https://doi.org/10.1016/S0009-2509(00)00436-X.
[54] S. Bellinghausen, Modelling and Scaling Rules of High-Shear Wet Granulation of Pharmaceuticals [PhD Thesis], University of Sheffield, 2020.
[55] G. Stoeckl, A. Atxutegi, S. Bellinghausen, S. Heinrich, Employing a multi-resonance microwave sensor for in-line moisture monitoring of fluidized bed agglomeration, Chem. Eng. J. 499 (2024) 156053, https://doi.org/10.1016/J.CEJ.2024.156053.
[56] C.Y. Wen, Y.H. Yu, A generalized method for predicting the minimum fluidization velocity, AIChE J. 12 (3) (1966) 610–612, https://doi.org/10.1002/aic.690120343.
[57] C. Goniva, C. Kloss, N.G. Deen, J.A.M. Kuipers, S. Pirker, Influence of rolling friction on single spout fluidized bed simulation, Particuology 10 (5) (2012) 582–591, https://doi.org/10.1016/j.partic.2012.05.002.
[58] C. Kloss, C. Goniva, A. Hager, S. Amberger, S. Pirker, Models, algorithms and validation for opensource DEM and CFD-DEM, Prog. Comput. Fluid Dyn. Int. J. 12 (2/3) (2012) 140, https://doi.org/10.1504/PCFD.2012.047457.
[59] H.G. Weller, G. Tabor, H. Jasak, C. Fureby, A tensorial approach to computational continuum mechanics using object-oriented techniques, Comput. Phys. 12 (6) (1998) 620–631, https://doi.org/10.1063/1.168744.
[60] Y. Tsuji, T. Tanaka, T. Ishida, Lagrangian numerical simulation of plug flow of cohesionless particles in a horizontal pipe, Powder Technol. 71 (3) (1992) 239–250, https://doi.org/10.1016/0032-5910(92)88030-L.
[61] J. Ai, J.-F. Chen, J.M. Rotter, J.Y. Ooi, Assessment of rolling resistance models in discrete element simulations, Powder Technol. 206 (3) (2011) 269–282, https://doi.org/10.1016/j.powtec.2010.09.030.
[62] R. Beetstra, M.A. van der Hoef, J.A.M. Kuipers, Drag force of intermediate Reynolds number flow past mono- and bidisperse arrays of spheres, AIChE J. 53 (2) (2007) 489–501, https://doi.org/10.1002/aic.11065.
[63] M. Hounslow, The population balance as a tool for understanding particle rate processes, Kona Powder Part. J. 16 (0) (1998) 179–193, https://doi.org/10.14356/kona.1998021.
[64] W.I.J. Kariuki, B. Freireich, R.M. Smith, M. Rhodes, K.P. Hapgood, Distribution nucleation: quantifying liquid distribution on the particle surface using the dimensionless particle coating number, Chem. Eng. Sci. 92 (2013) 134–145, https://doi.org/10.1016/j.ces.2013.01.010.
[65] S. Palzer, The effect of glass transition on the desired and undesired agglomeration of amorphous food powders, Chem. Eng. Sci. 60 (14) (2005) 3959–3968, https://doi.org/10.1016/j.ces.2005.02.015.
[66] F. Bunke, S. Pietsch-Braune, S. Heinrich, Three-dimensional measurement method of binary particle collisions under dry and wet conditions, Chem. Eng. J. 489 (2024) 151016, https://doi.org/10.1016/J.CEJ.2024.151016.
[67] M. Oh, C.C. Pantelides, A modelling and simulation language for combined lumped and distributed parameter systems, Comput. Chem. Eng. 20 (6–7) (1996) 611–633, https://doi.org/10.1016/0098-1354(95)00196-4.
[68] V.S. Vassiliadis, R.W.H. Sargent, C.C. Pantelides, Solution of a class of multistage dynamic optimization problems. 1. Problems without path constraints, Ind. Eng. Chem. Res. 33 (9) (1994) 2111–2122, https://doi.org/10.1021/ie00033a014.
[69] V.S. Vassiliadis, R.W.H. Sargent, C.C. Pantelides, Solution of a class of multistage dynamic optimization problems. 2. Problems with path constraints, Ind. Eng. Chem. Res. 33 (9) (1994) 2123–2133, https://doi.org/10.1021/ie00033a015.
[70] J. Burgschweiger, E. Tsotsas, Experimental investigation and modelling of continuous fluidized bed drying under steady-state and dynamic conditions, Chem. Eng. Sci. 57 (24) (2002) 5021–5038, https://doi.org/10.1016/S0009-2509(02)00424-4.
[71] W.E. Ranz, W.R. Marshall, Evaporation from drops, Chem. Eng. Prog. 48 (1952) 141–146.
[72] S. Brunauer, P.H. Emmett, E. Teller, Adsorption of gases in multimolecular layers, J. Am. Chem. Soc. 60 (2) (1938) 309–319, https://doi.org/10.1021/ja01269a023.
[73] L. Vogel, W. Peukert, Breakage behaviour of different materials—construction of a mastercurve for the breakage probability, Powder Technol. 129 (1–3) (2003) 101–110, https://doi.org/10.1016/S0032-5910(02)00217-6.
[74] L. Vogel, W. Peukert, From single particle impact behaviour to modelling of impact mills, Chem. Eng. Sci. 60 (18) (2005) 5164–5176, https://doi.org/10.1016/j.ces.2005.03.064.